

ASC Report No. 17/2012

# **Transient Schrödinger-Poisson simulations of a high-frequency resonant tunneling diode oscillator**

J.-F. Mennemann, A. Jüngel, and H. Kosina

Institute for Analysis and Scientific Computing  
Vienna University of Technology — TU Wien  
[www.asc.tuwien.ac.at](http://www.asc.tuwien.ac.at) ISBN 978-3-902627-05-6

## Most recent ASC Reports

- 16/2012 *N. Zamponi and A. Jüngel*  
Two spinorial drift-diffusion models for quantum electron transport in graphene
- 15/2012 *M. Aurada, M. Feischl, T. Führer, M. Karkulik, D. Praetorius*  
Efficiency and optimality of some weighted-residual error estimator for adaptive 2D boundary element methods
- 14/2012 *I. Higuera, N. Happenhofer, O. Koch, and F. Kupka*  
Optimized Imex Runge-Kutta methods for simulations in astrophysics: A detailed study
- 13/2012 *H. Woracek*  
Asymptotics of eigenvalues for a class of singular Krein strings
- 12/2012 *H. Winkler, H. Woracek*  
A growth condition for Hamiltonian systems related with Krein strings
- 11/2012 *B. Schörkhuber, T. Meurer, and A. Jüngel*  
Flatness-based trajectory planning for semilinear parabolic PDEs
- 10/2012 *M. Karkulik, D. Pavlicek, and D. Praetorius*  
On 2D newest vertex bisection: Optimality of mesh-closure and  $H^1$ -stability of  $L_2$ -projection
- 09/2012 *J. Schöberl and C. Lehrenfeld*  
Domain Decomposition Preconditioning for High Order Hybrid Discontinuous Galerkin Methods on Tetrahedral Meshes
- 08/2012 *M. Aurada, M. Feischl, T. Führer, M. Karkulik, J.M. Melenk, D. Praetorius*  
Classical FEM-BEM coupling methods: nonlinearities, well-posedness, and adaptivity
- 07/2012 *M. Aurada, M. Feischl, T. Führer, M. Karkulik, J.M. Melenk, D. Praetorius*  
Inverse estimates for elliptic integral operators and application to the adaptive coupling of FEM and BEM

Institute for Analysis and Scientific Computing  
Vienna University of Technology  
Wiedner Hauptstraße 8–10  
1040 Wien, Austria

**E-Mail:** [admin@asc.tuwien.ac.at](mailto:admin@asc.tuwien.ac.at)  
**WWW:** <http://www.asc.tuwien.ac.at>  
**FAX:** +43-1-58801-10196

ISBN 978-3-902627-05-6

© Alle Rechte vorbehalten. Nachdruck nur mit Genehmigung des Autors.



# TRANSIENT SCHRÖDINGER-POISSON SIMULATIONS OF A HIGH-FREQUENCY RESONANT TUNNELING DIODE OSCILLATOR

JAN-FREDERIK MENNEMANN, ANSGAR JÜNGEL, AND HANS KOSINA

**ABSTRACT.** Transient simulations of a resonant tunneling diode oscillator are presented. The semiconductor model for the diode consists of a set of time-dependent Schrödinger equations coupled to the Poisson equation for the electric potential. The one-dimensional Schrödinger equations are discretized by the finite-difference Crank-Nicolson scheme using memory-type transparent boundary conditions which model the injection of electrons from the reservoirs. An efficient recursive algorithm due to Arnold, Ehrhardt, and Sofronov is used to implement the transparent boundary conditions, enabling simulations which involve a large number of time steps. Special care has been taken to provide a discretization of the boundary data which is completely consistent with the underlying finite-difference scheme. The transient regime between two stationary states and the self-oscillatory behavior of an oscillator circuit, containing a resonant tunneling diode, is simulated.

## 1. INTRODUCTION

The resonant tunneling diode has a wide variety of applications as a high-frequency and low-consumption oscillator or switch. The resonant tunneling structure is usually treated as an open quantum system with two large reservoirs and an active region containing a double-barrier heterostructure. Accurate time-dependent simulations are of great importance to develop efficient and reliable quantum devices and to reduce their development time and cost. There exist several approaches in the literature to model a resonant tunneling diode. The simplest approach is to replace the diode by an equivalent circuit containing nonlinear current-voltage characteristics [20]. Another approximation is to employ the Wannier envelope function development [21]. Other physics-based approaches rely on the Wigner equation [7, 19], the nonequilibrium Green's function theory [10, 18], quantum hydrodynamic models [12, 13, 16], and the Schrödinger equation [6, 8, 22, 23].

In this paper, we adopt the latter approach and simulate the time-dependent behavior of a resonant tunneling diode using the Schrödinger-Poisson system in one space dimension. In this setting, the electrons are assumed to be in a mixed state with Fermi-Dirac statistics and the electrostatic interaction is taken into account at the Hartree level. Each state is determined as the solution of the transient Schrödinger equation with nonhomogeneous

---

*Date:* May 11, 2012.

*2000 Mathematics Subject Classification.* 65M06, 35Q40, 82D37.

*Key words and phrases.* Schrödinger-Poisson system, transient simulations, discrete transparent boundary conditions, resonant tunneling diode.

The first two authors acknowledge partial support from the Austrian Science Fund (FWF), grants P20214, P22108, and I395, and the Austrian-French Project of the Austrian Exchange Service (ÖAD)..

transparent boundary conditions. The Schrödinger equations are discretized by the Crank-Nicolson finite difference scheme and coupled self-consistently to the Poisson equation.

The numerical challenges result from the large number of Schrödinger equations which have to be solved, accounting for the energy distribution of the incoming electrons. Each state is provided with transparent boundary conditions, which raises the computational costs sharply. Further, we consider time-dependent and possibly smoothly varying applied voltages. Their implementation is more involved than voltages which are constant or change instantaneously in time.

Homogeneous discrete transparent boundary conditions for the Crank-Nicolson discretization of the time-dependent Schrödinger equation were derived in [1]. The inhomogeneous case for a transient scattering problem is considered in [2] where the exterior potentials are allowed to switch instantaneously in time. However, realistic device simulations require more flexible descriptions of the applied potential. It is well known that, using a suitable gauge change, one can get rid of the transient potential. Corresponding inhomogeneous transparent boundary conditions can be found in [5]. In numerical simulations, however, we observed that these boundary conditions may lead to unphysical distortions in the conduction current density. The reason is that the discretization of the gauge change term is not consistent with the underlying finite-difference method. Therefore, we suggest a discretization which is derived from the Crank-Nicolson time integration scheme. Our approach completely removes these numerical artifacts and we show that the total current density is now perfectly conserved. The discretization is completely consistent with the underlying Crank-Nicolson scheme inheriting its conservation and stability properties. In addition, our approach requires to compute a single set of convolutions coefficients (instead of two), which simplifies the implementation.

To cope with the large number of Schrödinger equations to be solved, we developed a parallel version of our solver utilizing multiple cores on shared memory processors. However, as the discrete transparent boundary conditions are of memory type, their numerical implementation requires to store (and use) the boundary data for all the past history. For this reason, simulations involving longer time scales are too costly. We solve this problem using a fast evaluation of the discrete transparent boundary conditions, based on an approximation of the discrete convolution kernel by sum-of-exponentials, which has been presented in [3]. To our knowledge, this rather new numerical technique has not been applied to real device simulations so far.

We present solutions to the Schrödinger-Poisson system for *large times* up to 100 ps (compared to 5 ps in [22], 6 ps in [8] and 8 ps in [5]) with reasonable computational effort. The numerical results allow us to identify plasma oscillations in a certain time regime of the resonant tunneling diode and to estimate the life time of the resonant state. Moreover, we present for the first time simulations of a *high-frequency oscillator circuit* containing a resonant tunneling diode, based on a full Schrödinger-Poisson solver with transparent boundary conditions. Simplified tunneling diode oscillator circuits have been considered in [20, 21, 24]. With our approach it is possible to observe quantities like the current or electron density inside the resonant tunneling diode directly. As an example, we illustrate

how the electron charge periodically enters and leaves the quantum well of the double barrier structure according to the frequency of the oscillator.

The paper is organized as follows. In Section 2, we detail the computation of the stationary states which are employed as the initial values for the transient simulations. The discretization of the stationary transparent boundary conditions is recalled and the iteration strategy for the electric potential (which is different from [5, 22]) is explained and discussed. The transient algorithm is detailed in Section 3. Numerical experiments for constant applied voltage, time-dependent applied voltage, and for an oscillator circuit are presented in Section 4.

## 2. STATIONARY SIMULATIONS

The steady state is the basis for the transient simulations. Therefore, we discuss first the stationary regime.

**2.1. Schrödinger-Poisson model.** We assume that the device is connected to left and right semi-infinite leads. The leads are assumed to be in thermal equilibrium and at constant potential. At the contacts, electrons are injected with some given profile. We suppose that the charge transport is ballistic and that the electron wave functions evolve independently from each other. The one-dimensional device consists of three regions: two highly doped regions,  $[0, a_1]$  and  $[a_6, L]$ , with the doping concentration  $n_D^1$  and a lowly doped region,  $[a_1, a_6]$ , with the doping density  $n_D^2$  (see Figure 1). The middle interval contains a double barrier, described by the barrier potential

$$V_{\text{barr}}(x) = \begin{cases} V_0 & \text{for } x \in [a_2, a_3] \cup [a_4, a_5], \\ 0 & \text{else.} \end{cases}$$

The doping profile  $n_D$  is defined by

$$n_D(x) = \begin{cases} n_D^1 & \text{for } x \in [0, a_1] \cup [a_6, L], \\ n_D^2 & \text{else.} \end{cases}$$

The parameters are taken from [5, 22]:

$$\begin{aligned} a_1 &= 50 \text{ nm}, & a_2 &= 60 \text{ nm}, & a_3 &= 65 \text{ nm}, \\ a_4 &= 70 \text{ nm}, & a_5 &= 75 \text{ nm}, & a_6 &= 85 \text{ nm}, \\ L &= 135 \text{ nm}, & n_D^1 &= 10^{24} \text{ m}^{-3}, & n_D^2 &= 5 \cdot 10^{21} \text{ m}^{-3}, \end{aligned}$$

and the barrier height is  $V_0 = 0.3 \text{ eV}$ .

The Coulomb interaction is taken into account at the Hartree level, i.e. by an infinite number of Schrödinger equations

$$(1) \quad -\frac{\hbar^2}{2m} \frac{d^2 \phi_k}{dx^2}(x) + V(x) \phi_k(x) = E(k) \phi_k(x), \quad x \in \mathbb{R},$$

self-consistently coupled to the Poisson equation,

$$(2) \quad \begin{aligned} -\frac{d^2 V_{\text{self}}}{dx^2} &= \frac{e^2}{\varepsilon} (n[V_{\text{self}}] - n_D), \quad x \in (0, L), \\ V_{\text{self}}(0) &= 0 \quad V_{\text{self}}(L) = -eU, \end{aligned}$$

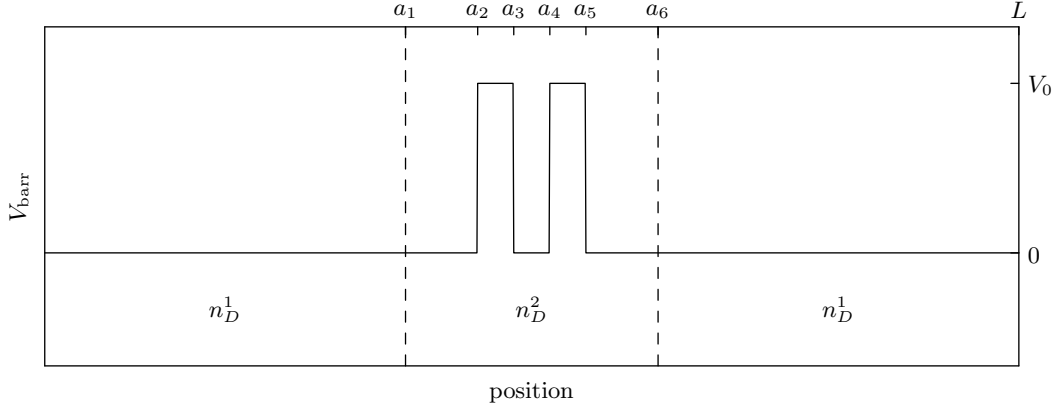


FIGURE 1. Barrier potential and doping profile of a double-barrier heterostructure.

where  $V = V_{\text{barr}} + V_{\text{self}}$  is the potential energy. The physical parameters are the reduced Planck constant  $\hbar$ , the effective electron mass  $m$ , the elementary charge  $e$ , and the permittivity  $\varepsilon = \varepsilon_r \varepsilon_0$ , being the product of the relative permittivity  $\varepsilon_r$  and the electric constant  $\varepsilon_0$ . Furthermore,  $U \geq 0$  denotes the applied voltage, and the electron density is defined by

$$(3) \quad n[V_{\text{self}}](x) = \int_{\mathbb{R}} g(k) |\phi_k(x)|^2 dk.$$

The injection profile  $g(k)$  is given according to Fermi-Dirac statistics by

$$(4) \quad g(k) = \frac{mk_B T_0}{2\pi^2 \hbar^2} \ln \left( 1 + \exp \left( \frac{E_F - \hbar^2 k^2 / (2m)}{k_B T_0} \right) \right),$$

where  $k_B$  is the Boltzmann constant,  $T_0$  the temperature of the semiconductor and  $E_F$  the Fermi energy (relative to the conduction band edge). In all subsequent simulations, we use, as in [22],  $\varepsilon_r = 11.44$ ,  $T_0 = 300$  K,  $E_F = 6.7097 \cdot 10^{-21}$  J, and the effective mass of Gallium arsenide,  $m = 0.067m_e$ , with  $m_e$  being the electron mass at rest.

In order to define the total electron energy  $E(k)$  depending on the wave number  $k \in \mathbb{R}$ , we need to distinguish the cases  $k > 0$  and  $k < 0$ . For  $k > 0$ , the electrons enter from the left, and we have  $E(k) = \hbar^2 k^2 / (2m)$ . The wave function in the leads is given by

$$\begin{aligned} \phi_k(x) &= e^{ikx} + r(k)e^{-ikx}, \quad x < 0, \\ \phi_k(x) &= t(k) \exp \left( i \sqrt{2m(E(k) - V(L)) / \hbar^2} x \right), \quad x > L. \end{aligned}$$

Eliminating the transmission and reflection coefficients  $t(k)$  and  $r(k)$ , respectively, the boundary conditions

$$(5) \quad \phi'_k(0) + ik\phi_k(0) = 2ik, \quad \phi'_k(L) = i \sqrt{2m(E(k) - V(L)) / \hbar^2} \phi_k(L)$$

follow. For  $k < 0$ , the electrons enter from the right. The total energy is given by  $E(k) = \hbar^2 k^2 / (2m) - eU$ , and the wave function in the leads reads as

$$\begin{aligned}\phi_k(x) &= t(k) \exp\left(-i\sqrt{2mE(k)/\hbar^2}x\right), \quad x < 0, \\ \phi_k(x) &= e^{ikx} + r(k)e^{-ikx}, \quad x > L.\end{aligned}$$

This yields the boundary conditions

$$(6) \quad \phi'_k(0) = -i\sqrt{2mE(k)/\hbar^2}\phi_k(0), \quad \phi'_k(L) + ik\phi_k(L) = 2ike^{ikL}.$$

Summarizing, the stationary problem consists in the Schrödinger equation (1) with the transparent boundary conditions (5)-(6) coupled to the Poisson equation (2) via the electron density (3).

**2.2. Discrete transparent boundary conditions.** We recall the finite-difference discretization of the stationary Schrödinger equation with transparent boundary conditions [2]. Using standard second-order finite differences on the equidistant grid  $x_j = j\Delta x$ ,  $j \in \{0, \dots, J\}$ , with  $x_J = L$  and  $\Delta x > 0$ , we find for the grid points located in the computational domain,

$$(7) \quad \phi_{j+1} - 2\phi_j + \phi_{j-1} + \frac{2m(\Delta x)^2}{\hbar^2}(E(k) - V_j)\phi_j = 0.$$

Usually, the boundaries are treated as follows: First, the analytical boundary conditions (5) and (6) are discretized using standard centered finite differences. Then the ghost points  $x_{-1} = -\Delta x$  and  $x_{J+1} = (J+1)\Delta x$  are eliminated via (7), which yields a second-order discretization of the analytical boundary conditions at  $x_0 = 0$  and  $x_J = L$ . It is important to note that this discretization may yield spurious oscillations in the numerical solution [2]. If one is interested in stationary calculations only, this poses no real problem as the error can easily be made small by choosing  $\Delta x$  sufficiently small. However, the stationary solutions will serve as initial states in our transient simulations. Therefore, we need to avoid any spurious oscillations, which would otherwise be propagated with every time step. For this, we derive the boundary conditions on the discrete level [2] consistent with the finite-difference discretization (7).

In the semi-infinite leads, the potential energy is assumed to be constant,  $V_j^\ell = 0$  for  $j \leq 0$  and  $V_j^r = -eU$  for  $j \geq L$ . Then, using  $\phi_j = \alpha^j$  as an ansatz in (7) with the constant potential  $V_j = V^{\ell,r}$ , we obtain a quadratic equation for  $\alpha$  with two solutions  $\alpha_{1,2}^\ell$  and  $\alpha_{1,2}^r$ , respectively:

$$\begin{aligned}\alpha_{1,2}^{\ell,r} &= 1 - \frac{m(E(k) - V^{\ell,r})(\Delta x)^2}{\hbar^2} \\ &\quad \pm i\sqrt{\frac{2m(E(k) - V^{\ell,r})(\Delta x)^2}{\hbar^2} - \frac{m^2(E(k) - V^{\ell,r})^2(\Delta x)^4}{\hbar^4}}.\end{aligned}$$

Here  $E(k) - V^{\ell,r}$  corresponds to the kinetic energy  $E_{\text{kin}}^{\ell,r}(k)$  in the left or right lead. In case  $E_{\text{kin}}^{\ell,r}(k) > 0$  the solution is a discrete plane wave and  $(\Delta x)^2 < 2\hbar^2/(m(E(k) - V^{\ell,r}))$  is needed to ensure  $|\alpha_{1,2}| = 1$ , which in practise is not a restriction. In case  $E_{\text{kin}}^{\ell,r}(k) = 0$

the solution is constant. Depending on the applied voltage,  $E_{\text{kin}}^{\ell,r}(k)$  might also become negative. In that case, the solution is decaying or growing exponentially fast and we select the decaying solution as it is the only physically reasonable solution.

In practice, we start with the calculation of the total energy  $E(k) = E_{\text{kin}}^{\ell,r}(k) + V^{\ell,r}$ . For electrons coming from the left contact we have  $E(k) = E_{\text{kin}}^{\ell}(k)$ . As the incoming electron is represented by a discrete plane wave,  $E_{\text{kin}}^{\ell}(k)$  is positive but depending on the applied voltage  $E_{\text{kin}}^r(k)$  might be positive, zero or negative. For electrons coming from the right contact, we have  $E(k) = E_{\text{kin}}^r(k) - eU$ . Again, the incoming wave function is a discrete plane wave, i.e.,  $E_{\text{kin}}^r(k) > 0$  but nothing is said about  $E_{\text{kin}}^{\ell}(k)$ . At this point it should be noted that the kinetic energy of the incoming electron needs to be computed according to the discrete dispersion relation

$$E_{\text{kin}}(k) = \frac{\hbar^2}{m(\Delta x)^2}(1 - \cos(k\Delta x)),$$

which follows after solving the centered finite-difference discretization of the free Schrödinger equation

$$-\frac{\hbar^2}{2m} \frac{d^2}{dx^2} e^{ikx} = E_{\text{kin}}(k) e^{ikx}.$$

In the limit  $\Delta x \rightarrow 0$ , we recover the continuous dispersion relation  $E_{\text{kin}}(k) = \hbar^2 k^2 / (2m)$ .

Let us consider a wave function entering the device from the left contact ( $k > 0$ ). For  $j \leq 0$ , the solution to (7) is a superposition of an incoming and a reflected discrete plane wave,  $\phi_j = \beta^j + B\beta^{-j}$  where  $\beta = \alpha_1^{\ell}$ . We eliminate  $B$  from  $\phi_{-1} = \beta^{-1} + B\beta$ ,  $\phi_0 = 1 + B$  to find the discrete transparent boundary condition at  $x_0$ :

$$-\beta^{-1}\phi_{-1} + \phi_0 = 1 - \beta^{-2}.$$

For  $j \geq L$ , the solution to (7) is given by  $\phi_j = C\gamma^j$  with  $\gamma = \alpha_1^r$ . This means that  $\phi_{J+1} = C\gamma^{J+1} = \gamma\phi_J$ , and the boundary condition at  $x_J$  becomes

$$\phi_J - \gamma^{-1}\phi_{J+1} = 0.$$

Summarizing, we obtain the linear system  $A\phi = b$  with the tridiagonal matrix  $A$  consisting of the main diagonal  $(-\beta^{-1}, -2 + 2m(\Delta x)^2(E(k) - V_0)/\hbar^2, \dots, -2 + 2m(\Delta x)^2(E(k) - V_J)/\hbar^2, -\gamma^{-1})$  and the first off diagonals  $(1, \dots, 1)$ . The vector of the unknowns is given by  $\phi = (\phi_{-1}, \dots, \phi_{J+1})^{\top}$  and  $b$  represents the right-hand side  $b = (1 - \beta^{-2}, 0, \dots, 0)^{\top}$ .

The case of a wave function entering from the right contact ( $k < 0$ ) works analogously.

**2.3. Solution of the Schrödinger-Poisson system.** We explain our strategy to solve the coupled Schrödinger-Poisson system. To this end, we introduce the equidistant energy grid

$$(8) \quad \mathcal{K} = \{-k_M, -k_M + \Delta k, \dots, -\Delta k, +\Delta k, \dots, k_M - \Delta k, k_M\}, \quad K := |\mathcal{K}|.$$

The electron density (3) is approximated by

$$n_{\text{disc}}[V_{\text{self}}](x) = \Delta k \sum_{k \in \mathcal{K}} g(k) |\phi_k(x)|^2,$$



where the Fermi-Dirac statistics  $g(k)$  is defined in (4) and the functions  $\phi_k$  are the scattering states, i.e., the solutions to the stationary Schrödinger equation (1) with the transparent boundary conditions (5) and (6), discretized as in Section 2.2. This approximation is reasonable if  $\Delta k$  is sufficiently small and  $k_M$  is sufficiently large. In the numerical simulations below, we choose  $K = 3000$  and, as in [5, Section 5],  $k_M = \sqrt{2m(E_F + 7k_B T_0)}/\hbar$ , recalling that  $E_F = 6.7097 \cdot 10^{-21}$  J and  $T_0 = 300$  K.

The discrete Schrödinger-Poisson system is iteratively solved as follows. We set  $V = V_{\text{barr}} + V_{\text{self},U}^{(\ell)}$ , where  $V_{\text{self},U}^{(\ell)}$  is the  $\ell$ -th iteration of  $V_{\text{self}}$  for the applied voltage  $U$ . Given  $V$ , we compute a set of quasi eigenstates  $\{\phi_k^{(\ell)}\}_{k \in \mathcal{K}}$ . This defines the discrete electron density

$$n_{\text{disc}}[V_{\text{self},U}^{(\ell)}] = \Delta k \sum_{k \in \mathcal{K}} g(k) |\phi_k^{(\ell)}(x)|^2.$$

The Poisson equation is solved by employing a Gummel-type method:

$$-\frac{d^2}{dx^2} V_{\text{self},U}^{(\ell+1)} = \frac{e^2}{\varepsilon} \left( n[V_{\text{self},U}^{(\ell)}] \exp \left( \frac{V_{\text{self},U}^{(\ell)} - V_{\text{self},U}^{(\ell+1)}}{V_{\text{self}}^{\text{ref}}} \right) - n_D \right),$$

$$V_{\text{self},U}^{(\ell+1)}(0) = 0, \quad V_{\text{self},U}^{(\ell+1)}(L) = -eU.$$

The parameter  $V_{\text{self}}^{\text{ref}}$  can be tuned to reduce the number of iterations; we found empirically that the choice  $V_{\text{self}}^{\text{ref}} = 0.04$  eV minimizes the iteration number. If the relative error in the  $\ell^2$ -norm is smaller than a fixed tolerance,

$$(9) \quad \left\| \frac{V_{\text{self},U}^{(\ell+1)} - V_{\text{self},U}^{(\ell)}}{V_{\text{self},U}^{(\ell+1)}} \right\|_2 \leq \delta,$$

we accept  $V_{\text{self}} := V_{\text{self},U}^{(\ell+1)}$  and  $\{\phi_k^{(\ell+1)}\}_{k \in \mathcal{K}}$  as the approximate self-consistent solution. Otherwise, we proceed with the iteration  $\ell + 1 \rightarrow \ell + 2$  and compute a new set of scattering states. The procedure is repeated until (9) is fulfilled. We have chosen the tolerance  $\delta = 10^{-6}$ . For the starting potential, it turns out that the choice  $V_{\text{self},0 \text{ mV}}^{(0)} = 0$  mV is sufficient. Only 7 iterations are needed until criterion (9) is fulfilled. As a result we obtain  $V_{\text{self},0 \text{ mV}}^{(7)}$ , which is depicted in Figure 2(a) (solid line).

Problems arise when non-equilibrium solutions are computed. For instance, let  $U = 1$  mV. In order to compute  $V_{\text{self}}$ , we set  $V_{\text{self},1 \text{ mV}}^{(0)} := V_{\text{self},0 \text{ mV}}^{(7)}$  to start the iteration process. The next iterations are illustrated in Figure 2(a) (dashed lines). They do not converge and are physically not realistic.

A possibility to overcome this problem is to use a slightly different description of the applied potential. To explain the idea, we decompose the potential energy as  $V = V_0 + V_1 + V_{\text{barr}}$ , where

$$-\frac{d^2 V_0}{dx^2} = 0 \quad \text{in } (0, L), \quad V_0(0) = 0, \quad V_0(L) = -eU,$$

$$-\frac{d^2 V_1}{dx^2} = \frac{e^2}{\varepsilon} (n - n_D) \quad \text{in } (0, L), \quad V_1(0) = 0, \quad V_1(L) = 0,$$

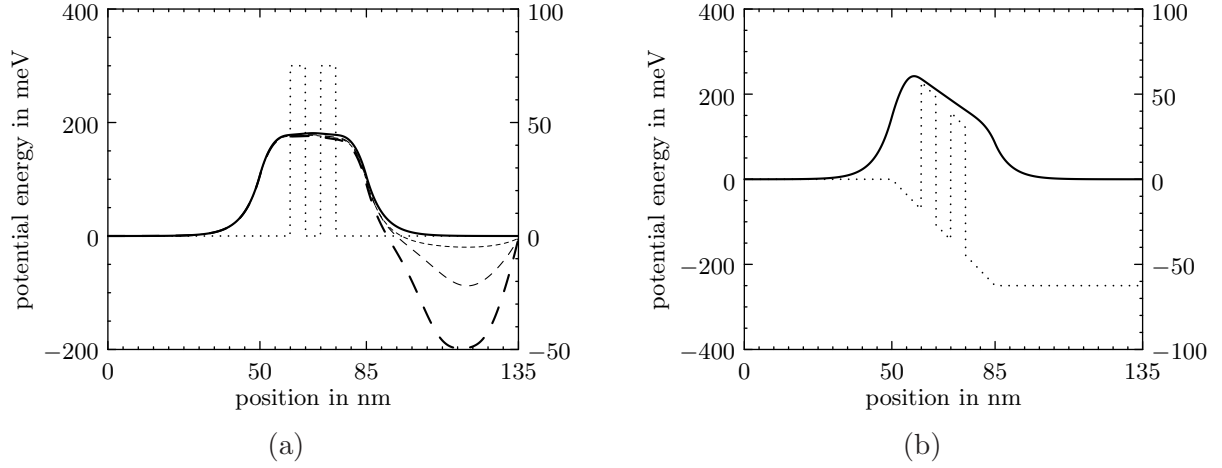


FIGURE 2. (a) Solid line: self-consistent solution for  $U = 0$  mV, found after 7 iterations. Dashed lines: divergent approximations for  $U = 1$  mV. Dotted line: barrier potential. (b) Solid line: self-consistent solution for  $U = 250$  mV according to approximation (10). Dotted line: sum of the barrier potential and a ramp-like potential.

i.e., the self-consistent potential is  $V_{\text{self}} = V_0 + V_1$ . The first boundary-value problem can be solved explicitly:  $V_0(x) = -eUx/L$ ,  $x \in [0, L]$ . This formulation is equivalent to the original problem with the same numerical difficulties. In order to overcome these problems, one may replace  $V_0$  by the ramp-like potential

$$(10) \quad \tilde{V}_0(x) = -B_0 \left( \frac{x - a_1}{a_6 - a_1} \mathbf{1}_{[a_1, a_6)} + \mathbf{1}_{[a_6, \infty)} \right), \quad x \in [0, L],$$

where  $\mathbf{1}_I$  is the characteristic function on the interval  $I \subset \mathbb{R}$ . This idea has been employed in, e.g., [5, 22] (see Figure 1 for the definition of  $a_1$  and  $a_6$ ). The function  $\tilde{V}_0 + V_{\text{barr}}$  is illustrated in Figure 2(b) (dotted line). The potential energy is then given by  $V = \tilde{V}_0 + V_1 + V_{\text{barr}}$ . With this approximation, the above Gummel iteration scheme for the Poisson equation for  $V_1$  converges without any problems, see Figure 2(b) (solid line), even for large applied voltages.

In this paper, we suggest another strategy which is consistent with the definition of the electric potential. Given the self-consistent solution  $V_{\text{self}, U}$  for the applied voltage  $U$ , we wish to compute a self-consistent solution with the applied voltage  $U + \Delta U$ . The idea is to define

$$(11) \quad V_{\text{self}, U + \Delta U}^{(0)}(x) := V_{\text{self}, U}(x) - \Delta U \frac{2x - L}{L} \mathbf{1}_{[L/2, L]}$$

to start the iteration. For  $U = 0$  mV and  $\Delta U = 25$  mV, the Gummel scheme converges to a physically reasonable solution after 7 iterations (i.e., (9) is fulfilled). Some iterations are shown in Figure 3. We observed that a voltage step  $\Delta U < 30$  mV leads to convergent solutions also for large applied voltages.

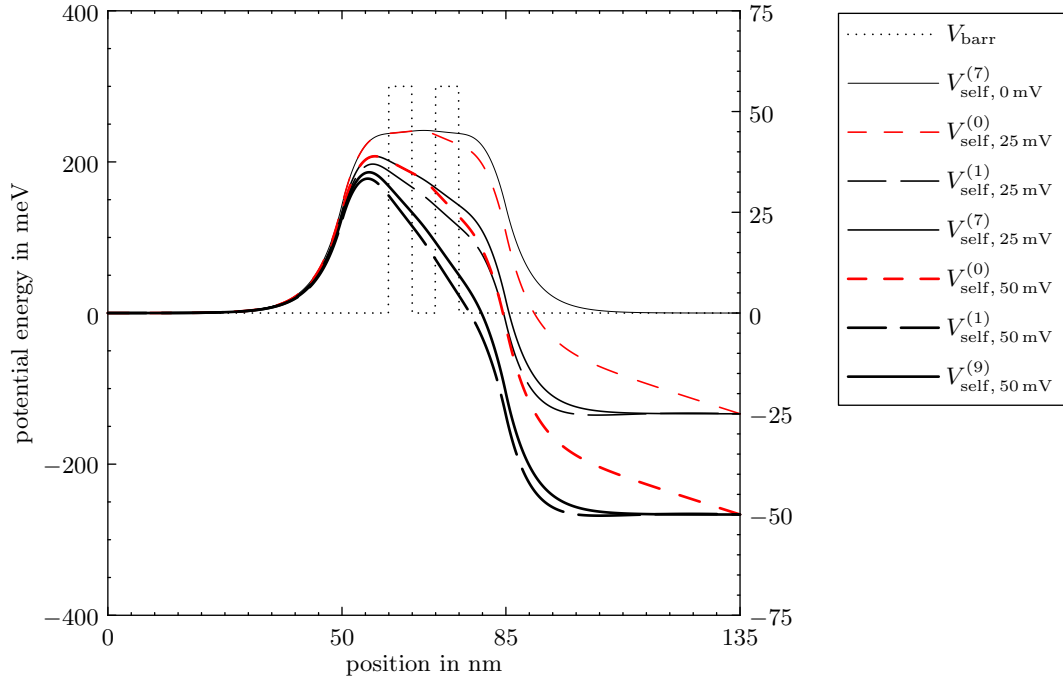


FIGURE 3. Some iterations computed according to (11).

Remarkably, both approaches (10) and (11) lead to rather different current-voltage characteristics as illustrated in Figure 4. Here, the (conduction) current density

$$(12) \quad J_{\text{cond}} = \frac{e\hbar}{m} \int_{\mathbb{R}} g(k) \text{Im} \left( \phi_k^* \frac{d\phi_k}{dx} \right) dk$$

is approximated by

$$J_{\text{disc}} = \frac{e\hbar}{m} \Delta k \sum_{k \in \mathcal{K}} g(k) \text{Im} \left( \phi_k^* \frac{d\phi_k}{dx} \right),$$

using symmetric finite differences to compute  $d\phi_k/dx$ .

Remarkably, the voltages at which the peak and valley current occur are quite different. For completeness, the electron density and potential energy, computed from our strategy, are presented in Figure 5. We observe the maximal space charge in the quantum well at the peak current, corresponding to the voltage  $U = 250$  mV.

Summarizing, we have been able to compute the self-consistent solution to the stationary Schrödinger-Poisson system using a consistent definition of the potential for large applied bias.

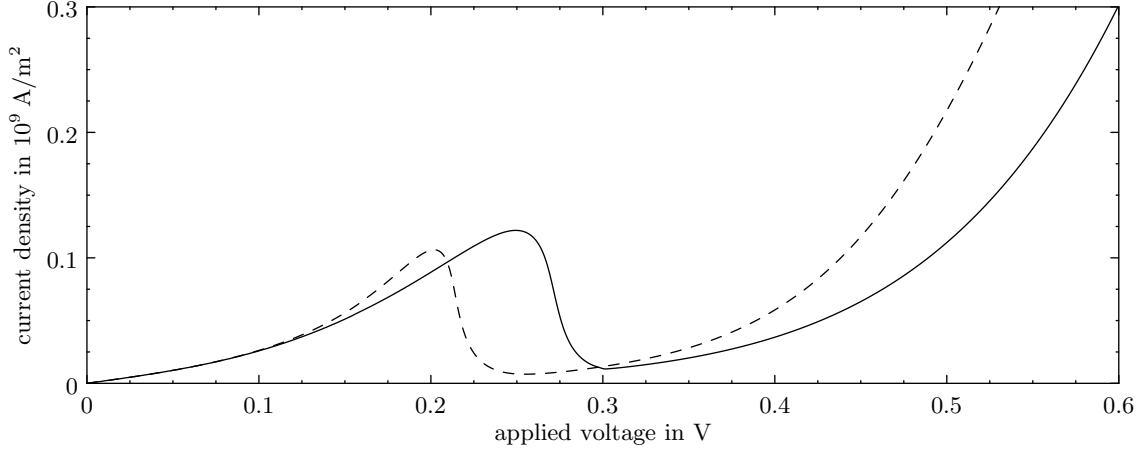


FIGURE 4. Current-voltage characteristics. The solid line corresponds to our calculation with the natural boundary condition  $V_{\text{self}}(L) = -eU$ . The dashed line is obtained with the ramp-like potential barrier approximation using  $V_{\text{self}}(L) = 0$ .

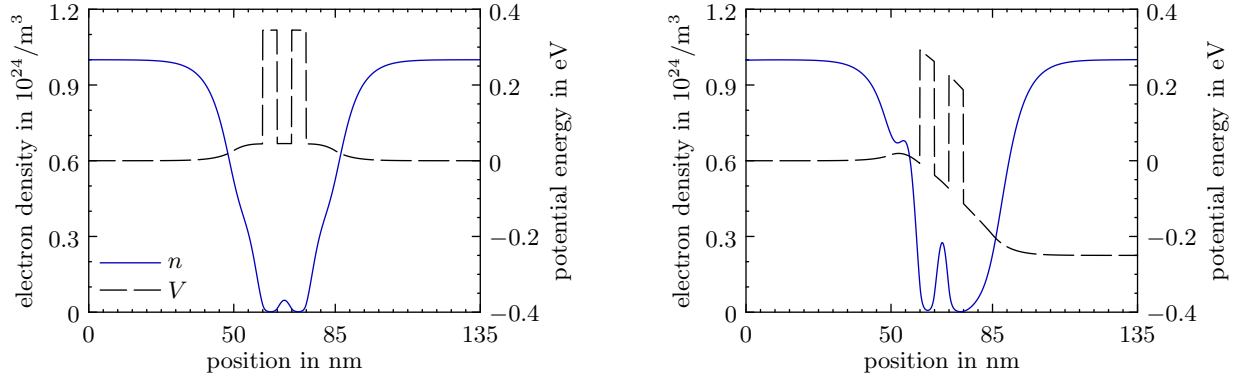


FIGURE 5. Electron density (solid line) and electric potential (dashed line) for an applied voltage of  $U = 0$  mV (left) and  $U = 250$  mV (right).

### 3. TRANSIENT SIMULATIONS

In this section, we detail the numerical discretization of the transient Schrödinger equations

$$(13) \quad i\hbar \frac{\partial \psi_k}{\partial t} = -\frac{\hbar^2}{2m} \frac{\partial^2 \psi_k}{\partial x^2} + V(\cdot, t)\psi_k, \quad \psi_k(\cdot, 0) = \phi_k, \quad x \in [0, L], \quad t > 0, \quad k \in \mathcal{K},$$

with transparent boundary conditions detailed below, where  $\mathcal{K}$  is defined in (8). To simplify the presentation, we skip in this section the index  $k$ .

**3.1. Nonhomogeneous discrete transparent boundary conditions.** The transient Schrödinger equation (13) is discretized by the commonly used Crank-Nicolson scheme:

$$(14) \quad \psi_{j-1}^{n+1} + \left(iR - 2 + wV_j^{n+1/2}\right) \psi_j^{n+1} + \psi_{j+1}^{n+1} = -\psi_{j-1}^n + \left(iR + 2 - wV_j^{n+1/2}\right) \psi_j^n - \psi_{j+1}^n,$$

where  $\psi_j^n$  approximates  $\psi(x_j, t_n)$  with  $x_j = j\Delta x$  and  $t_n = n\Delta t$  ( $j \in \mathbb{Z}$ ,  $n \in \mathbb{N}_0$ ),  $V_j^{n+1/2}$  approximates  $V(j\Delta x, (n+1/2)\Delta t)$ , and  $R = 4m(\Delta x)^2/(\hbar\Delta t)$ ,  $w = -2m(\Delta x)^2/\hbar^2$ . Under the assumptions that the initial wave function is compactly supported in  $(0, L)$  and that the applied voltage vanishes,  $V(x, t) = 0$  for  $x \leq 0$  and  $x \geq L$ ,  $t \geq 0$ , it is well known (see, e.g., [2, 4]) that transparent boundary conditions for the Schrödinger equation (13) read as

$$(15a) \quad \frac{\partial \psi}{\partial x}(0, t) = \sqrt{\frac{2m}{\pi\hbar}} e^{-i\pi/4} \frac{d}{dt} \int_0^t \frac{\psi(0, \tau)}{\sqrt{t-\tau}} d\tau,$$

$$(15b) \quad \frac{\partial \psi}{\partial x}(L, t) = -\sqrt{\frac{2m}{\pi\hbar}} e^{-i\pi/4} \frac{d}{dt} \int_0^t \frac{\psi(L, \tau)}{\sqrt{t-\tau}} d\tau.$$

The (homogeneous) discrete transparent boundary conditions, based on the above Crank-Nicolson scheme, are given as follows [1]:

$$(16a) \quad \psi_1^{n+1} - s^{(0)}\psi_0^{n+1} = \sum_{\ell=1}^n s^{(n+1-\ell)}\psi_0^\ell - \psi_1^n, \quad n \geq 0,$$

$$(16b) \quad \psi_{J-1}^{n+1} - s^{(0)}\psi_J^{n+1} = \sum_{\ell=1}^n s^{(n+1-\ell)}\psi_J^\ell - \psi_{J-1}^n, \quad n \geq 0,$$

with the convolution coefficients

$$(17) \quad s^{(n)} = \left(1 - i\frac{R}{2}\right) \delta_{n,0} + \left(1 + i\frac{R}{2}\right) \delta_{n,1} + \alpha e^{-in\varphi} \frac{P_n(\mu) - P_{n-2}(\mu)}{2n-1}$$

and the abbreviations

$$\varphi = \arctan \frac{4}{R}, \quad \mu = \frac{R}{\sqrt{R^2 + 16}}, \quad \alpha = \frac{i}{2} \sqrt[4]{R^2(R^2 + 16)} e^{i\varphi/2}.$$

Here,  $P_n$  denotes the  $n$ th-degree Legendre polynomial ( $P_{-1} = P_{-2} = 0$ ), and  $\delta_{n,j}$  is the Kronecker symbol. The Crank-Nicolson scheme along with these discrete boundary conditions yields an unconditionally stable discretization which is perfectly reflection-free [1, 2].

Next, let the initial wave function be a solution to the stationary Schrödinger equation with energy  $E$  and let the exterior potential at the right contact be given by a time-dependent function,  $V(x, t) = -eU(t)$  for  $x \geq L$ ,  $t \geq 0$ . This leads to nonhomogeneous transparent boundary conditions. We describe our strategy to discretize these boundary conditions. Our approach is motivated by that presented in [5, Appendix B], but we suggest, similarly as in [2], a discretization of the gauge change which is consistent with the underlying finite-difference scheme. Additionally, our approach requires only a single set of convolution coefficients instead of two.

First, we derive a nonhomogeneous discrete transparent boundary condition at  $x_j = L$ . To this end, we consider the difference between the unknown wave function  $\psi$  and the time evolution of the scattering state,  $\phi(x) \exp(iEt/\hbar)$ , in the right lead  $[L, \infty)$ . We employ a gauge change to get rid of the time-dependent potential  $V_L(t) = -eU(t)$ . As a consequence, the function  $\psi(x, t) \exp(i \int_0^t V_L(s) ds/\hbar)$  solves the free transient Schrödinger equation in  $[L, \infty)$ . Using a similar gauge change, a straightforward computation shows that  $\phi(x) \exp(-i(E - V_L(0))t/\hbar)$  solves the free Schrödinger equation in  $[L, \infty)$  as well. Hence,

$$(18) \quad \varphi(x, t) := \psi(x, t) \exp\left(\frac{i}{\hbar} \int_0^t V_L(s) ds\right) - \phi(x) \exp\left(-\frac{i}{\hbar}(E - V_L(0))t\right)$$

for  $x \in [L, \infty)$  solves the free transient Schrödinger equation. Furthermore,  $\phi(x, 0) = 0$  for all  $x \in [L, \infty)$ . Therefore, we could apply (15b) to derive a nonhomogeneous transparent boundary condition at the right contact. Instead we replace  $\varphi(x, t)$  by some approximation  $\varphi_j^n$  and subsequently apply (16b) to derive a discrete boundary condition consistent with the Crank-Nicolson scheme.

The question is how to approximate the quantities  $\exp(i \int_0^t V_L(s) ds/\hbar)$  and  $\exp(-i(E - V_L(0))t/\hbar)$ . Indeed, the ad-hoc discretization for  $t = t_n$ ,

$$(19) \quad \begin{aligned} \exp\left(\frac{i}{\hbar} \int_0^t V_L(s) ds\right) &\approx \exp\left(\frac{i}{\hbar} \sum_{\ell=0}^{n-1} \frac{1}{2}(V_L^\ell + V_L^{\ell+1})\Delta t\right), \\ \exp\left(-\frac{i}{\hbar}(E - V_L(0))t\right) &= \exp\left(-\frac{i}{\hbar}(E - V_L(0))n\Delta t\right), \end{aligned}$$

where  $V_L^\ell = V_L(t_\ell)$ , is not consistent with the underlying finite-difference discretization, causing unphysical numerical reflections at the boundary. In principle, these reflections can be made arbitrarily small for  $\Delta t \rightarrow 0$ . However, for practical timestep sizes, the calculation of the current density would be still distorted. Our idea is to apply a Crank-Nicolson discretization to a differential equation satisfied by  $\exp(i \int_0^t V_L(s) ds/\hbar)$ . Indeed, this expression solves

$$\frac{d\varepsilon}{dt}(t) = \frac{i}{\hbar} V_L(t) \varepsilon(t), \quad \varepsilon(0) = 1.$$

The Crank-Nicolson discretization of this ordinary differential equation reads as

$$\varepsilon^{n+1} = \varepsilon^n + \Delta t \frac{i}{2\hbar} V_L^{n+1/2} (\varepsilon^{n+1} + \varepsilon^n), \quad \varepsilon^0 = 1.$$

This recursion relation can be solved explicitly yielding

$$\varepsilon^n = \exp\left(2i \sum_{\ell=0}^{n-1} \arctan\left(\frac{\Delta t}{2\hbar} V_L^{\ell+1/2}\right)\right), \quad n \in \mathbb{N}_0.$$

Analogously,  $\exp(-i(E - V_L(0))t/\hbar)$  is approximated by

$$\begin{aligned}\gamma_J^n &:= \exp\left(2i \sum_{\ell=0}^{n-1} \arctan\left(-\frac{\Delta t}{2\hbar} E\right)\right) \exp\left(2i \sum_{\ell=0}^{n-1} \arctan\left(\frac{\Delta t}{2\hbar} V_L(0)\right)\right) \\ &= \exp\left[2in \left(\arctan\left(\frac{\Delta t}{2\hbar} V_L(0)\right) - \arctan\left(\frac{\Delta t}{2\hbar} E\right)\right)\right], \quad n \in \mathbb{N}_0.\end{aligned}$$

Thus, definition (18) for  $\varphi$  can be approximated by

$$\varphi_j^n = \psi_j^n \varepsilon^n - \phi_j \gamma_J^n, \quad j \in \{0, \dots, J\}, \quad n \in \mathbb{N}_0.$$

Replacing  $\psi_j^n$  by  $\varphi_j^n$  in (16b), we obtain the desired nonhomogeneous discrete transparent boundary condition at  $x_J = L$ :

$$\begin{aligned}(20) \quad \psi_{J-1}^{n+1} \varepsilon^{n+1} - s^{(0)} \psi_J^{n+1} \varepsilon^{n+1} &= -\varepsilon^n \psi_{J-1}^n + \sum_{\ell=1}^n s^{(n+1-\ell)} (\psi_J^\ell \varepsilon^\ell - \phi_J \gamma_J^\ell) \\ &\quad - s^{(0)} \phi_J \gamma_J^{n+1} + \phi_{J-1} (\gamma_J^{n+1} + \gamma_J^n).\end{aligned}$$

At the left contact  $x_0 = 0$ , a nonhomogeneous boundary condition can be derived in a similar way. Since the potential energy in the left lead is assumed to vanish, the term  $\varepsilon^n$  is not needed, and the boundary condition is given by

$$\begin{aligned}(21) \quad \psi_1^{n+1} - s^{(0)} \psi_0^{n+1} &= -\psi_1^n + \sum_{\ell=1}^n s^{(n+1-\ell)} (\psi_0^\ell - \phi_0 \gamma_0^\ell) \\ &\quad - s^{(0)} \phi_0 \gamma_0^{n+1} + \phi_1 (\gamma_0^{n+1} + \gamma_0^n),\end{aligned}$$

where

$$\gamma_0^n := \exp\left(-2in \arctan\left(\frac{\Delta t}{2\hbar} E\right)\right), \quad n \in \mathbb{N}_0.$$

We summarize: The Crank-Nicolson scheme (14) with the nonhomogeneous discrete transparent boundary conditions (20) and (21) reads as

$$(22) \quad B\psi^{n+1} = C\psi^n + d^n,$$

where  $\psi^n = (\psi_0^n, \dots, \psi_J^n)^\top$ ,  $d = (d_0^n, 0, \dots, 0, d_J^n)^\top$ . Furthermore,  $B$  is a tridiagonal matrix with main diagonal  $(-s^{(0)}, iR - 2 + wV_1^{n+1/2}, \dots, iR - 2 + wV_{J-1}^{n+1/2}, -s^{(0)}\varepsilon^{n+1})$ , upper diagonal  $(1, \dots, 1)$ , and lower diagonal  $(1, \dots, 1, \varepsilon^{n+1})$ ;  $C$  is a tridiagonal matrix with main diagonal  $(0, iR + 2 - wV_1^{n+1/2}, \dots, iR + 2 - wV_{J-1}^{n+1/2}, 0)$ , upper diagonal  $(-1, \dots, -1)$  and lower diagonal  $(-1, \dots, -1, -\varepsilon^n)$ ; furthermore,

$$(23) \quad d_0^n = \sum_{\ell=1}^n s^{(n+1-\ell)} (\psi_0^\ell - \phi_0 \gamma_0^\ell) - s^{(0)} \phi_0 \gamma_0^{n+1} + \phi_1 (\gamma_0^{n+1} + \gamma_0^n),$$

$$(24) \quad d_J^n = \sum_{\ell=1}^n s^{(n+1-\ell)} (\psi_J^\ell \varepsilon^\ell - \phi_J \gamma_J^\ell) - s^{(0)} \phi_J \gamma_J^{n+1} + \phi_{J-1} (\gamma_J^{n+1} + \gamma_J^n).$$

**3.2. Fast evaluation of the discrete convolution terms.** In the subsequent simulations, scheme (22) needs to be solved in each time step and for every wave function  $\psi = \psi_k$ ,  $k \in \mathcal{K}$ . Let  $N$  denote the number of time steps. For each  $k \in \mathcal{K}$ , we require order  $O(N)$  storage units and  $O(N^2)$  work units to compute the discrete convolutions in (23) and (24). For this reason, simulations with several ten thousands of time steps are not feasible. To overcome this problem, one may truncate the convolutions at some index, since the decay rate of the convolution coefficients is of order  $O(n^{-3/2})$  [11, Section 3.3]. The drawback of this approach is that still several hundred of convolution terms are necessary to avoid unphysical reflections at the boundaries.

The basic idea of [3] is to approximate the original convolution coefficients  $s^{(n)}$  by

$$\tilde{s}^{(n)} := \begin{cases} s^{(n)}, & n < \nu, \\ \sum_{\ell=1}^{\Lambda} b_{\ell} q_{\ell}^{-n}, & n \geq \nu, \end{cases}$$

such that

$$(25) \quad \mathcal{C}^{(n)}(u) := \sum_{\ell=1}^{n-\nu} \tilde{s}^{(n-\ell)} u^{\ell} \approx \sum_{\ell=1}^{n-\nu} s^{(n-\ell)} u^{\ell}$$

can be evaluated by a recurrence formula which reduces the numerical effort drastically. As in [3], we set  $\nu = 2$  to exclude  $s^{(0)}$  and  $s^{(1)}$  from the approximation. In fact,  $s^{(0)}$  does not appear in the original convolutions, whereas  $s^{(1)}$  is excluded to increase the accuracy.

Let  $\Lambda \in \mathbb{N}$ . The set  $\{b_0, q_0, \dots, b_{\Lambda}, q_{\Lambda}\}$  is computed as follows. First, define the formal power series

$$h(x) := s^{(\nu)} + s^{(\nu+1)}x + s^{(\nu+2)}x^2 + \dots + s^{(\nu+2\Lambda-1)}x^{\nu+2\Lambda-1} + \dots, \quad |x| \leq 1.$$

The first (at least  $2\Lambda$ ) coefficients are required to calculate the  $[\Lambda-1|\Lambda]$ -Padé approximation of  $h$ ,  $\tilde{h}(x) := P_{\Lambda-1}(x)/Q_{\Lambda}(x)$ , where  $P_{\Lambda-1}$  and  $Q_{\Lambda}$  are polynomials of degree  $\Lambda-1$  and  $\Lambda$ , respectively. If this approximation exists, we can compute its Taylor series  $\tilde{h}(x) = \tilde{s}^{(\nu)} + \tilde{s}^{(\nu+1)}x + \dots$ , and by definition of the Padé approximation, it holds that

$$\tilde{s}^{(n)} = s^{(n)} \quad \text{for all } n \in \{\nu, \nu+1, \dots, \nu+2\Lambda-1\}.$$

It can be shown that, if  $Q_{\Lambda}$  has  $\Lambda$  simple roots  $q_{\ell}$  with  $|q_{\ell}| > 1$  for all  $\ell \in \{1, \dots, \Lambda\}$ , the approximated coefficients are given by

$$(26) \quad \tilde{s}^{(n)} = \sum_{\ell=1}^{\Lambda} b_{\ell} q_{\ell}^{-n}, \quad b_{\ell} := -\frac{P_{\Lambda-1}(q_{\ell})}{Q'_{\Lambda}(q_{\ell})} q_{\ell}^{\nu-1} \neq 0, \quad n \geq \nu, \quad \ell \in \{1, \dots, \Lambda\}.$$

Summarizing, one first computes the exact coefficients  $s^{(0)}, \dots, s^{(\nu+2\Lambda-1)}$  followed by the  $[\Lambda-1|\Lambda]$ -Padé approximation. Then one determines the roots of  $Q_{\Lambda}$ , yielding the numbers  $q_1, \dots, q_{\Lambda}$ . Finally, one evaluates (26) to find the coefficients  $b_0, \dots, b_{\Lambda}$ . We stress the fact that these calculations have to be performed with high precision ( $2\Lambda-1$  mantissa length) since otherwise the Padé approximation may fail (see [3]). We employ the Python library `mpmath` for arbitrary-precision floating-point arithmetics [15]. As an alternative, one may use the `Maple` script from [3, Appendix].



A particular feature of this approximation is that it can be calculated by recursion. More precisely, for  $n \geq \nu + 1$ , the function  $\mathcal{C}^{(n)}(u)$  in (25) can be written as

$$\mathcal{C}^{(n)}(u) = \sum_{\ell=1}^{\Lambda} C_{\ell}^{(n)}(u),$$

with

$$C_{\ell}^{(n)}(u) = q_{\ell}^{-1} C_{\ell}^{(n-1)}(u) + b_{\ell} q_{\ell}^{-2} u^{n-2}, \quad n \geq \nu + 1, \quad C_{\ell}^{(\nu)}(u) = 0.$$

Hence, the discrete convolutions (23) and (24) are approximated for  $n \geq \nu = 2$  by

$$\sum_{\ell=1}^n s^{(n+1-\ell)} u^{\ell} \approx \mathcal{C}^{(n+1)}(u) + s^{(1)} u^n,$$

whereas the exact expressions are used for  $n = 0$  and  $n = 1$ . As a result, the storage for the implementation of the transparent boundary conditions reduces from  $O(N)$  to  $O(\Lambda)$ . Even more importantly, the work is of order  $O(\Lambda N)$  instead of  $O(N^2)$ .

Obviously, the quality of the approximation depends on  $\Lambda$ . By construction, we have  $s^{(n)} = \tilde{s}^{(n)}$  for all  $n \in \{0, \dots, 2\Lambda + \nu - 1\}$  but  $\tilde{s}^{(n)}$  approximates  $s^{(n)}$  very well even if  $n$  is much larger [3]. As a result, a relatively small  $\Lambda$  is sufficient to obtain excellent results. In numerical tests, we found that the results from a computation using  $\Lambda > 24$  are indistinguishable (in a graphical representation) from the results obtained with the exact coefficients. This holds true for the evolution of single electron wavefunctions (regardless of their energy) as well as for the complete transient algorithm of Section 3.3 involving a very large number of time steps. Thus, using  $\Lambda = 32$ , we practically obtain perfect transparent boundary conditions.

**3.3. The complete transient algorithm.** In the previous sections, we have explained the approximation of the transient Schrödinger equation with transparent boundary conditions for given potential energy  $V = V_{\text{barr}} + V_{\text{self}}$ . Here, we make explicit the coupling procedure with the Poisson equation for the selfconsistent potential

$$-\frac{\partial^2 V_{\text{self}}}{\partial x^2} = \frac{e^2}{\varepsilon} (n[V_{\text{self}}] - n_D), \quad x \in (0, L), \quad V_{\text{self}}(0, t) = 0, \quad V_{\text{self}}(L, t) = -eU(t),$$

with the electron density

$$n[V_{\text{self}}](x, t) = \int_{\mathbb{R}} g(k) |\psi_k(x, t)|^2 dk.$$

According to the Crank-Nicolson scheme, a natural approach would be to employ a two-step predictor-corrector scheme. More precisely, let  $\{\psi_k^n\}_{k \in \mathcal{K}} \rightarrow \{\psi_k^*\}_{k \in \mathcal{K}}$  be propagated for one time step using  $V_{\text{self}}^{(n)}$  to obtain  $V_{\text{self}}^{(*)}$ . Then one uses  $V_{\text{self}}^{(n+1/2)} := \frac{1}{2}(V_{\text{self}}^{(n)} + V_{\text{self}}^{(*)})$  to propagate  $\{\psi_k^n\}_{k \in \mathcal{K}} \rightarrow \{\psi_k^{n+1}\}_{k \in \mathcal{K}}$  again. This procedure doubles the numerical effort and is computationally too costly. As an alternative, the scheme  $V_{\text{self}}^{(n+1/2)} := 2V_{\text{self}}^{(n)} - V_{\text{self}}^{(n-1/2)}$  can be employed (as in [22]). We found in our simulations that the most simple approach,  $V_{\text{self}}^{(n+1/2)} := V_{\text{self}}^{(n)}$ , gives essentially the same results as the above schemes. The reason is probably that the electron density evolves very slowly and hence, the variations  $V_{\text{self}}$  are

small. Similarly, the right boundary condition of the Poisson equation can be replaced by  $V_{\text{self}}(L) = -eU(t_n)$  if the applied voltage varies slowly. This is used in the circuit simulations of Section 4.3.

Our complete transient algorithm is presented in Figure 6.

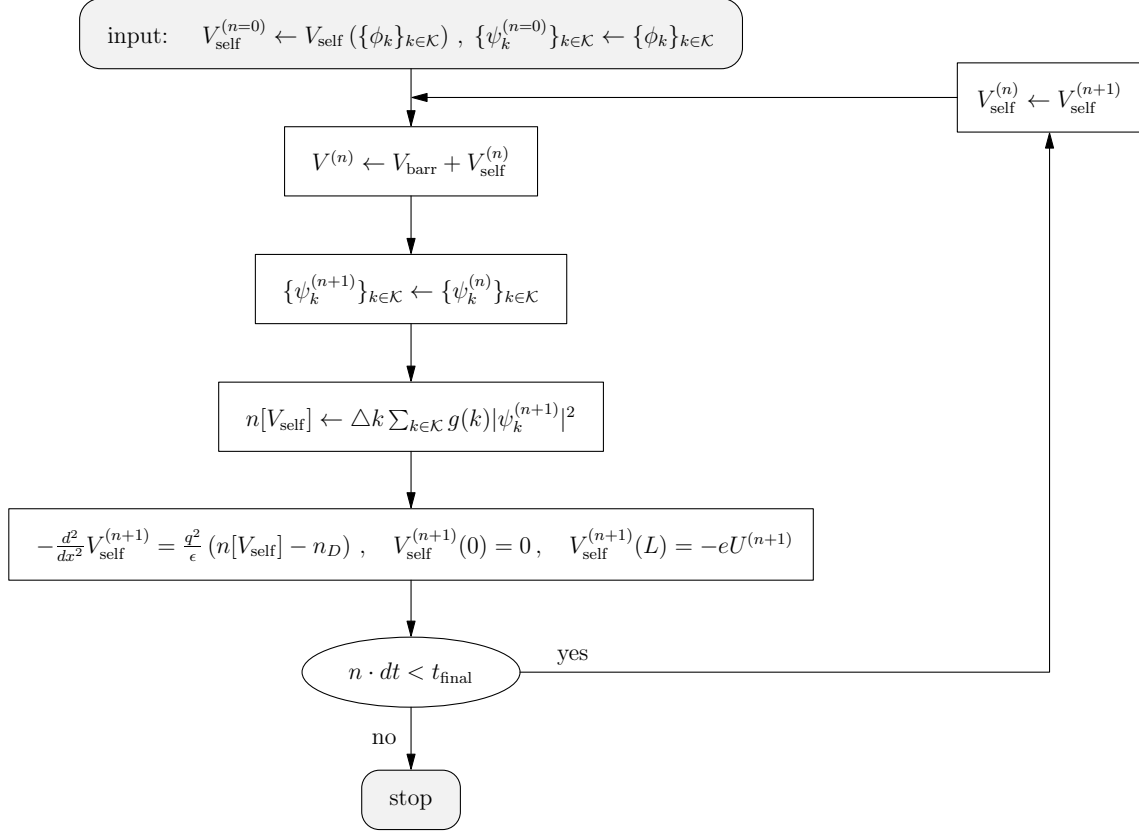


FIGURE 6. Flow chart of the transient scheme.

**3.4. Details of the implementation.** The final solver is implemented in the C++ programming language using the matrix library **Eigen** [14] for concise and efficient computations. If not stated otherwise, we compute  $K = 3000$  wave functions. The space grid size is chosen to be  $\Delta x = 0.1$  nm, which corresponds to  $J + 1 = 1351$  spatial grid points. The time step size is  $\Delta t = 1$  fs. With the maximal kinetic energy of injected electrons  $\hbar\omega_M = \hbar^2 k_M^2 / (2m)$  (see Section 2.3 for the definition of the maximal wave number  $k_M$ ), the period is computed according to  $\tau_M = 2\pi / \omega_M$ . Thus, one wave oscillation is resolved by  $\tau_M / \Delta t \approx 18.5$  points. This shows that, in the finite-difference context, the time step size of  $\Delta t = 1$  fs cannot be chosen much larger. We note that this choice was also used in [22].

As we are interested in simulations with a very large number of time steps  $N$  (e.g.,  $N = 100\,000$ ), some sort of parallelization is indispensable. We employ the library **threads** to realize multiple threads on multi-core processors with shared memory. The most time

consuming part in the transient algorithm (see Section 3.3) is the propagation of the wave functions and the calculation of the electron density. Since the wave functions evolve independently of each other, this task can be easily parallelized. At every time step, we create a certain number of threads (usually, this number equals the number of cores available). To each thread, we assign a subset of wave functions which are propagated as described above. Before the threads are joined again, each thread computes its part of the electron density. All these parts provide the total electron density which is used to solve the Poisson equation in serial mode. The simulations presented below have been carried out on an Intel Core 2 Quad CPU Q9950 with  $4 \times 2.8$  GHz.

#### 4. NUMERICAL EXPERIMENTS

We present three numerical examples. The first example shows the importance to provide a complete consistent discretization of the open Schrödinger-Poisson system. The second numerical test shows the time-dependent behavior of a resonant tunneling diode, which allows us to identify three physical regions. Finally, the third experiment is concerned with the self-oscillatory behavior of a tunneling diode in a small electric circuit.

**4.1. First experiment: Constant applied potential.** The aim of the first numerical experiment is to demonstrate the importance that the complete numerical discretization has to be consistent with the underlying finite-difference scheme. To this end, we compute the stationary solution to the Schrödinger-Poisson system with an applied voltage of  $U = 250$  mV. At this voltage, the current density achieves its first maximum (see Figure 4). We apply the transient algorithm of section 3 until  $t = 25$  fs, keeping the applied voltage constant. Accordingly, the stationary solution should be preserved and the current density  $J_{\text{cond}}$ , defined in (12), is expected to be spatially constant.

The ad-hoc discretization (19) is employed using the time step sizes  $\Delta t = 1$  fs, 0.5 fs, 0.25 fs. We observe in Figure 7 that the current density is not constant. The reason is that the discretization (19) is not consistent with the underlying finite-difference scheme. The distortions are reduced for very small time step sizes but this leads to computationally expensive algorithms. In contrast, with the discrete gauge change of Section 3.1, the current density is perfectly constant even for the rather large time step  $\Delta t = 1$  fs; see Figure 7.

We mention that the transient solution is also distorted if the scattering states as initial wave functions are computed from an ad-hoc discretization of the continuous boundary conditions (5) and (6). For stationary computations, spurious reflections due to an inconsistent discretization play a minor role but they become a major issue for transient simulations.

**4.2. Second experiment: Time-dependent applied potential.** For the second numerical experiment, we consider a time-dependent applied voltage. The conduction current density is no longer constant but the total current density is expected to be conserved. We recall that the total current density  $J_{\text{tot}} = J_{\text{cond}} + \partial D / \partial t$  is the sum of the conduction current density  $J_{\text{cond}}$  and the displacement current density  $\partial D / \partial t$ . Here  $D$  denotes the

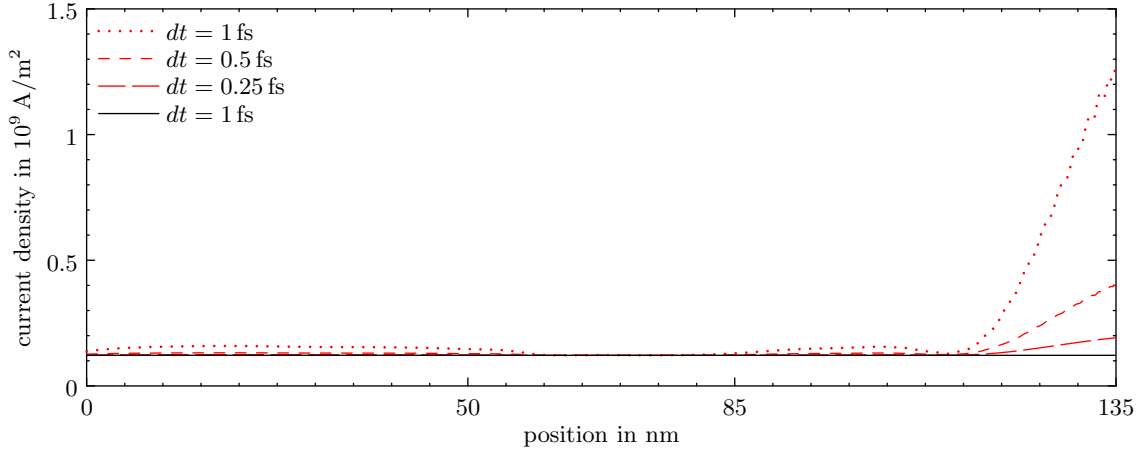


FIGURE 7. Conduction current density in a resonant tunneling diode at  $t = 25$  fs for a constant applied voltage of  $U = 250$  mV. Discretizations which are not completely consistent with the underlying finite-difference scheme yield strongly distorted numerical solutions (broken lines). In contrast, the conduction current density computed with our solver is perfectly constant (solid line).

electric displacement field which is related to the electric field  $E$  by  $D = \epsilon_0 \epsilon_r E$ . Replacing the electric field by the negative gradient of the potential we obtain

$$\frac{\partial D}{\partial t} = -\frac{\epsilon_0 \epsilon_r}{e} \frac{\partial}{\partial t} \nabla V_{\text{self}}.$$

The temporal and spatial derivatives are approximated using centered finite differences. Ampère's circuital law  $\nabla \times H = J_{\text{tot}}$  for the magnetic field strength  $H$  yields

$$\text{div } J_{\text{tot}} = \text{div}(\nabla \times H) = 0,$$

and hence, in one space dimension,  $J_{\text{tot}}$  is constant in space.

The following simulation demonstrates that the total current density is a conserved quantity in the discrete system as well. First, we compute the equilibrium state using an applied voltage of  $U = 0$  V. This solution is then propagated using a raised cosine function for the applied voltage

$$U(t) = \frac{U_0}{2} \left( 1 - \cos \frac{2\pi t}{T} \right), \quad 0 \leq t \leq 1 \text{ ps},$$

where  $U_0 = 0.25$  V and  $T = 2$  ps. At later times,  $t \geq 1$  ps,  $U(t) = U_0$  is kept constant. Conduction, displacement, and total current density at different times are depicted in the left column of Figure 8. As can be seen, the total current density is perfectly conserved at all considered times. The change of the charge density  $\partial \rho / \partial t$  is illustrated in the right column of Figure 8. In our model,  $\rho$  is given by  $\rho = e(n_D - n)$ .

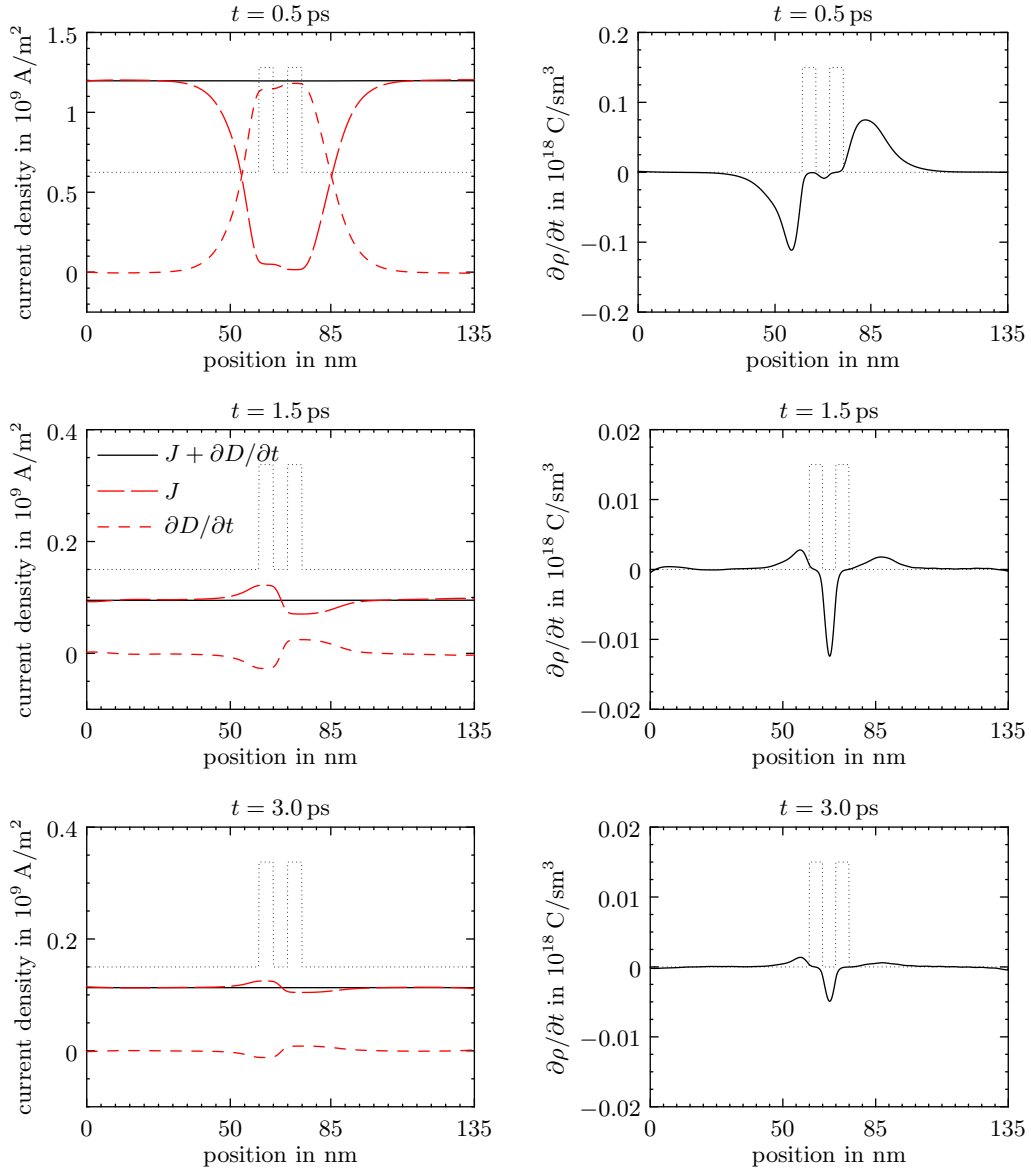


FIGURE 8. Left column: Total current density  $J_{\text{tot}} = J_{\text{cond}} + \partial D/\partial t$ , conduction current density  $J := J_{\text{cond}}$ , and displacement current density  $\partial D/\partial t$  versus position at different times. Right column: Temporal variation of the charge density  $\partial\rho/\partial t$  versus position.

The time-dependence of the total current density in response to the applied voltage is shown in Fig. 9. We can identify three different regions in the temporal behaviour, each of which is governed by a different physical mechanism.

*Region I: Capacitive behavior.* When the applied voltage increases during the first picosecond, the resonant tunneling diode behaves mainly like a parallel plate capacitor. This can

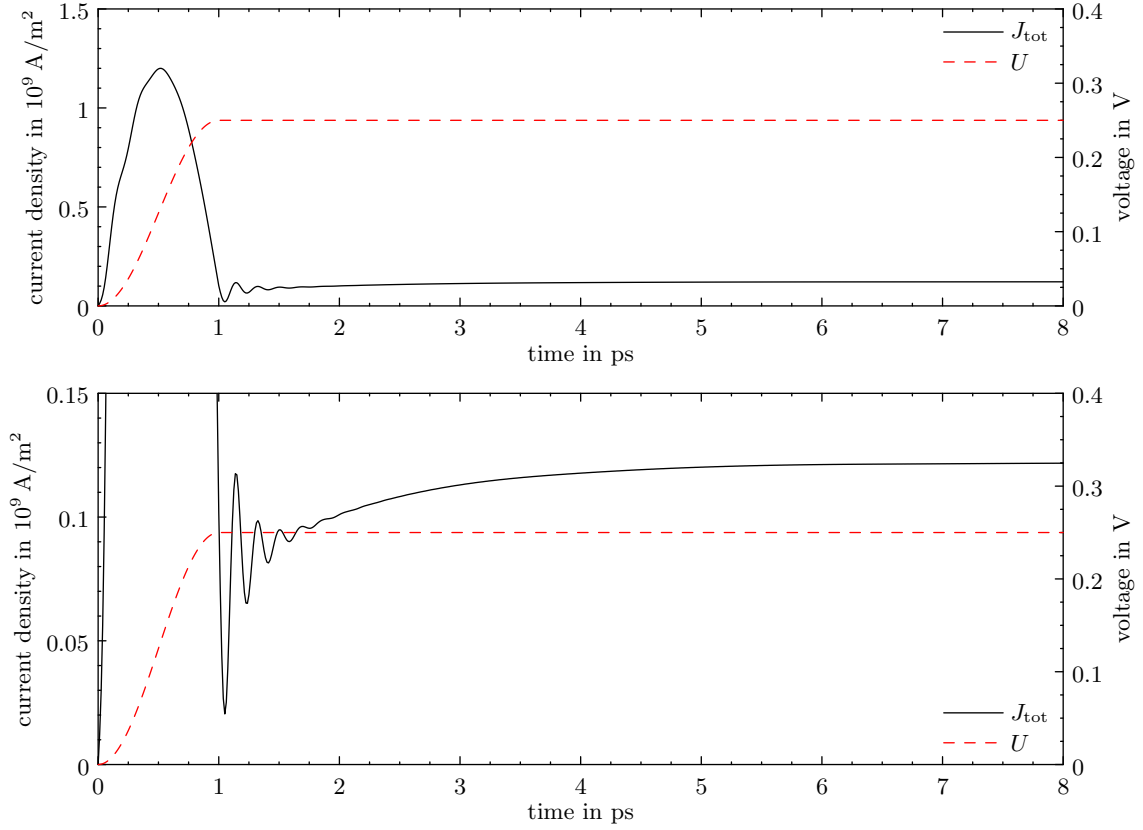


FIGURE 9. Applied voltage and total current density versus time in different scalings.

be clearly seen in the top left panel of Figure 8. In the region of the double barrier, the displacement current gives the dominant contribution to the total current, whereas the conduction current is small. The top right panel of Figure 8 shows a build-up of negative charge before the left barrier and of positive charge after the right barrier. The formation of opposite charges on the two sides of the double barrier results in the formation of an electric field between the two regions of opposite charge density. This field is necessary to accomodate the externally applied voltage. Figure 9 shows that the current closely follows the time derivative of the applied voltage:

$$J_{\text{cond}} \approx C \frac{dU}{dt} = \frac{\pi C U_0}{T} \sin\left(\frac{2\pi t}{T}\right).$$

This expression allows us to estimate the apparent capacitance  $C$ . The maximum current density occurring at  $t = T/4 = 0.5$  ps takes approximately the value  $1.2 \cdot 10^9 \text{ Am}^{-2}$ . We compute  $C = TJ/\pi U_0 = 3.06 \cdot 10^{-3} \text{ Fm}^{-2}$ . Equating this value to the parallel plate capacitance,  $C = \varepsilon_0 \varepsilon_r / d$ , we find the average separation of the opposite charge densities to be  $d = 33.1 \text{ nm}$ .

*Region II: Plasma oscillations.* During the second picosecond, a strongly damped oscillation occurs in the current density. From Figure 9, we estimate five oscillations to occur during one picosecond, which relates to a period of about 200 fs. It is believed that these are plasma oscillations which were excited by the rapidly changing applied voltage  $U$ . As soon as the transient phase of  $U(t)$  is over and  $U(t)$  is kept constant at  $U_0$  for  $t \geq 1$  ps, the excitation vanishes and the oscillations fade out quickly. As a rough estimate we calculate the plasma frequency  $\omega_p$  for a classical electron system of uniform density:

$$\omega_p^2 = \frac{ne^2}{m\varepsilon_0}.$$

Note that in the resonant tunneling diode the density is neither uniform nor is it governed by the classical equations of motion. Nevertheless, we may use this expression to estimate the order of magnitude of the time constant associated with this effect. Since plasma oscillations usually occur in the high-density regions of a device, we set  $n = n_D^1 = 10^{24} \text{ m}^{-3}$  and obtain  $\tau_p = 2\pi/\omega_p = 111.4 \text{ fs}$ . This value is of the same order as the 200 ps estimated above, which is a strong indication that the physical effect observed here is a plasma oscillation.

*Region III: Charging of the quantum well.* For  $t > 2$  ps, an exponential increase in the current can be clearly observed in Figure 9. Below 2 ps we see a superposition of both the exponential current increase and the plasma oscillations. The origin of this effect can be understood from the right panels of Figure 8. Negative charge builds up in the quantum well. This charge results from electrons tunneling through the left barrier into the quantum well. In this context, we note that the temporal variation of the voltage between the left and right end points  $a_2$  and  $a_5$  of the double-barrier structure, respectively, follows closely the variation of the applied voltage  $U$  and hence, it is practically constant for  $t > 1$  ps (see Figure 10). The rate  $|\partial\rho/\partial t|$  decreases with time as can be seen by the snapshots at  $t = 1.5$  ps and  $t = 3$  ps. We calculate the number of electrons residing in the quantum well:

$$N(t) := \int_{a_2}^{a_5} n(x, t) dx.$$

Since the charging process is expected to show an exponential time dependence, we assume the following exponential law for  $N(t)$  and extract the free parameters  $\tau$  and  $N_\infty$ :

$$N(t) = N_\infty + (N(t_1) - N_\infty) e^{-(t-t_1)/\tau}.$$

In Figure 10, the difference  $|N(t) - N_\infty|$  is plotted, which decays to zero with an extracted time constant of  $\tau = 1.25$  ps.

This time scale is related to the life time of a quasi-bound state. At  $U = 0.25$  V, the current-voltage characteristic has its first maximum, which means that the first resonant state in the quantum well is carrying the current. The life time of this resonant state can be extracted from the width of the resonance peak in the transmission coefficient. Figure 11 depicts the transmission coefficient of the double-barrier structure at  $U = 0$  V and  $U = 0.25$  V. The transmission coefficient is defined as the ratio between the transmitted

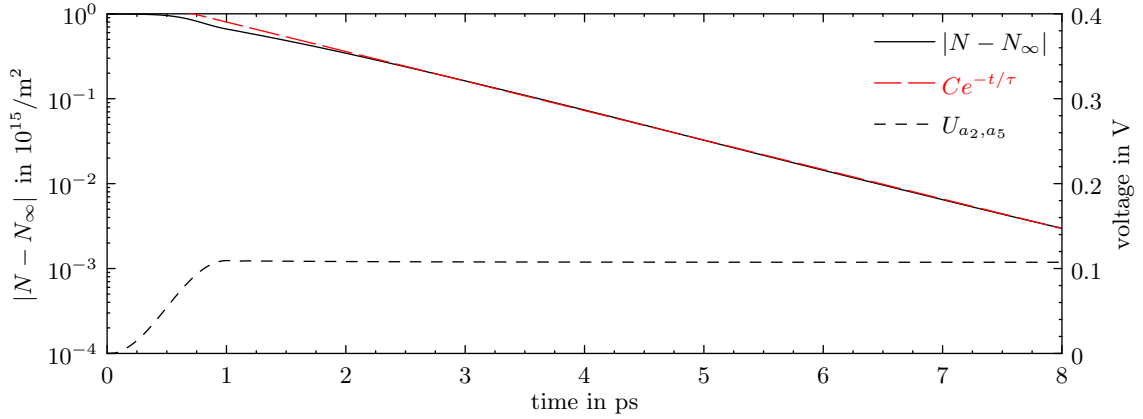


FIGURE 10. Number of electrons in the quantum well versus time. In Region III ( $t \geq 2$  ps) this number clearly follows an exponential law.  $U_{a_2, a_5}$  denotes the temporal variation of the voltage between  $x = a_2$  and  $x = a_5$ .

and the incident probability current density  $j_{\text{trans}}$  and  $j_{\text{inc}}$ . In terms of the amplitude and the wavenumber of the transmitted and the incident wave, it reads:

$$\frac{|j_{\text{trans}}|}{|j_{\text{inc}}|} = \frac{|A_{\text{trans}}|^2 k_{\text{trans}}}{|A_{\text{inc}}|^2 k_{\text{inc}}}.$$

Extracting  $\Delta E$ , the half width at half maximum of the first transmission peak, the life time of the resonant state can be estimated as follows [17]:

$$\tau = \frac{\hbar}{2\Delta E}.$$

At  $U = 0.25$  V we find that  $2\Delta E = 5.31 \cdot 10^{-4}$  eV and thus  $\tau = 1.24$  ps. This value is very close to the time constant of  $\tau = 1.25$  ps extracted from the exponential charge increase in the quantum well, which is the cause for the observed exponential current increase.

**4.3. Third experiment: Circuit simulations.** In this section, we simulate a high-frequency oscillator consisting of a voltage source  $U_e$ , a resistor with resistance  $R$ , an inductor with inductance  $L$ , a capacitor with capacity  $C$ , and a resonant tunneling diode RTD; see Figure 12. Each element of the circuit yields one current-voltage relationship,

$$(27) \quad U_R = RI_R, \quad U_L = L\dot{I}_L, \quad I_C = C\dot{U}_C, \quad I_{\text{RTD}} = f(U_{\text{RTD}}).$$

The last expression is to be understood as follows. Given the applied voltage  $U_{\text{RTD}}$  at the tunneling diode, the current  $I_{\text{RTD}}(t) = AJ_{\text{tot}}(t)$  is computed from the solution of the time-dependent Schrödinger-Poisson system. Here,  $A = 10^{-11} \text{ m}^{-3}$  is the cross sectional area of the diode and  $J_{\text{tot}}$  is the total current density. In the simulations we use  $R = 5 \Omega$ ,  $L = 50 \text{ pH}$ , and  $C = 10 \text{ fF}$ .

According to the Kirchhoff circuit laws, we have

$$(28) \quad U_e = U_R + U_{\text{RTD}} + U_L, \quad U_{\text{RTD}} = U_C, \quad I_L = I_R, \quad I_L = I_{\text{RTD}} + I_C.$$



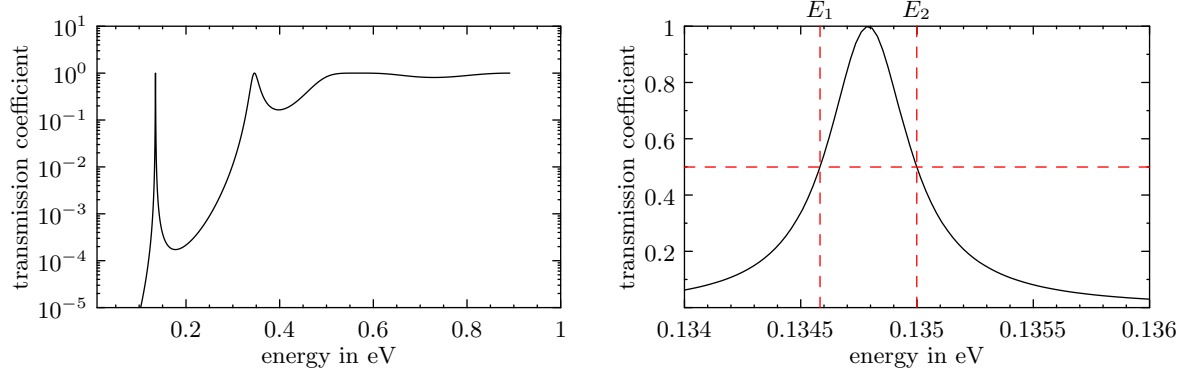
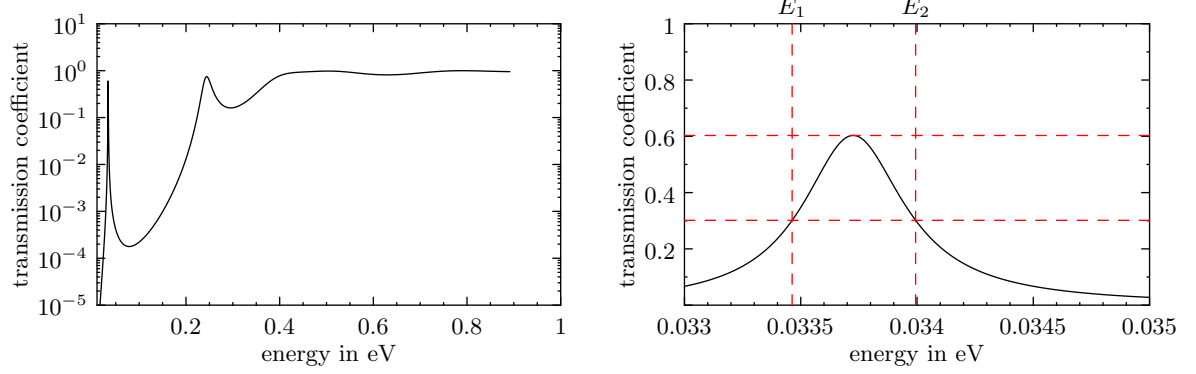
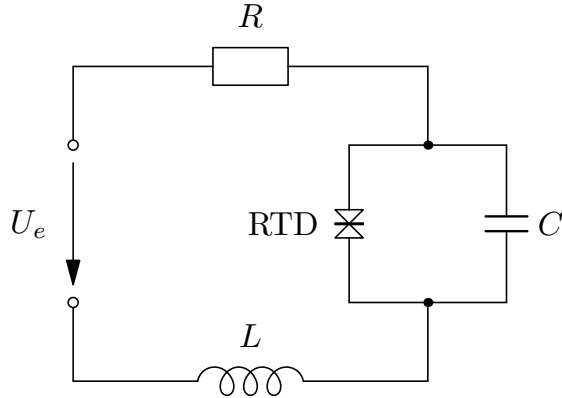
(a)  $U = 0$  mV(b)  $U = 250$  mVFIGURE 11. Transmission coefficient of the double-barrier structure at  $U = 0$  V and  $U = 0.25$  V in different scalings.

FIGURE 12. High-frequency oscillator containing the resonant tunneling diode RTD.

Combining (27) and (28), we find that

$$\begin{aligned} C\dot{U}_{\text{RTD}} &= C\dot{U}_C = I_C = I_L - I_{\text{RTD}}, \\ L\dot{I}_L &= U_L = U_e - U_R - U_{\text{RTD}} = U_e - RI_R - U_{\text{RTD}} = U_e - RI_L - U_{\text{RTD}}. \end{aligned}$$

Consequently, we obtain a system of two coupled ordinary differential equations,

$$(29) \quad \frac{d}{dt} \begin{pmatrix} U_{\text{RTD}} \\ I_L \end{pmatrix} = \begin{pmatrix} 0 & \frac{1}{C} \\ -\frac{1}{L} & -\frac{R}{L} \end{pmatrix} \begin{pmatrix} U_{\text{RTD}} \\ I_L \end{pmatrix} + \begin{pmatrix} -\frac{1}{C}I_{\text{RTD}} \\ \frac{1}{L}U_e(t) \end{pmatrix}.$$

The time-step size  $\Delta t$  is very small compared to the time scale of the variation of the potential energy and the variation of the current flowing through the diode. Hence, using the same time step for the time integration of (29), we can resort to an explicit time-stepping method. We choose the simplest one, the explicit Euler method. Alternatively, one may employ an implicit method, but we observed that both methods yield essentially the same results.

*First circuit simulation.* In the first simulation, the RTD solver is initialized with the steady state corresponding to  $U_{\text{RTD}}(t) = 0$  for all  $t \leq 0$ . The external voltage  $U_e$  is assumed to be zero for  $t \leq 0$ , and the initial conditions for (29) are  $U_{\text{RTD}}(0) = 0$  and  $I_L(0) = 0$ . For  $t \in [10, 20]$  ps, the external voltage is increased smoothly to 0.275 V and then kept constant (see Figure 13). This value is between the voltages where the stationary current density reaches its local maximum and minimum (see Figure 4). The time evolution of the voltage and the current at the RTD are depicted in Figure 13. It is clearly visible that the system starts to oscillate. Furthermore, the potential energy, electron density, current densities, and the temporal variation of the total charge  $\partial\rho/\partial t$  are shown in Figure 14 for four different times from the interval  $[t_1 = 77.7, t_2 = 87.2]$  ps, which covers exactly one oscillation. Around 2 ps after the beginning of the period, the electron density within the quantum well in  $[65, 70]$  nm becomes minimal (first row). After some time, we observe a build-up of negative charge in the quantum well with  $\partial\rho/\partial t < 0$  (second row). At about  $t = 84.6$  ps the electron density reaches its maximum value (third row). Subsequently, the electrons leave the quantum well again and  $\partial\rho/\partial t > 0$  in  $[65, 70]$  nm (fourth row). The frequency of the oscillations is approximately 105 GHz which corresponds qualitatively to frequencies observed in standard double-barrier tunneling diodes [9].

*Second circuit simulation.* In this experiment, the external voltage  $U_e$  is kept fixed for all times. At times  $t \leq 0$ , the circuit contains the voltage source, resistor, and RTD only. We initialize the transient Schrödinger-Poisson solver with the steady state corresponding to  $U_{\text{RTD}}(t) = 0.275$  V for all  $t \leq 0$ . To compensate for the voltage drop at the resistor, the external voltage is set to

$$U_e(t) = RI_{\text{RTD}}(t) + U_{\text{RTD}}(t), \quad t \leq 0.$$

At time  $t = 0$ , the capacitor and inductor are added to the circuit. In order to avoid discontinuities in the voltages, we charge the capacitor with the same voltage which is applied at the RTD before the switching takes place,  $U_C(t) = U_{\text{RTD}}(t)$  for  $t \leq 0$ . For similar reasons, we set the current flowing through the inductor to the current flowing

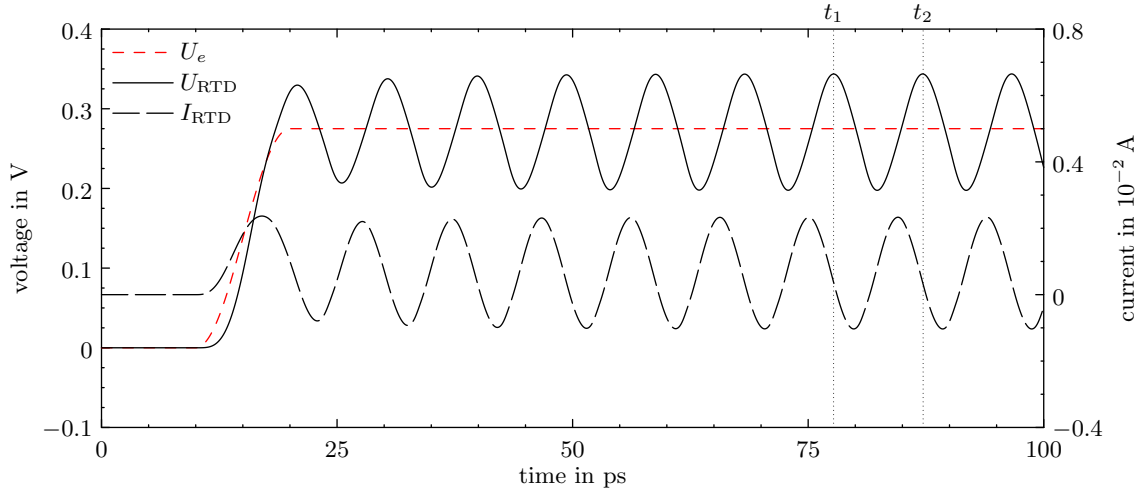


FIGURE 13. First circuit simulation: Voltage  $U_{\text{RTD}}$  and current  $I_{\text{RTD}}$  through the resonant tunneling diode versus time.

through the RTD,  $I_L(t) = I_{\text{RTD}}(t)$  for  $t \leq 0$ . This configuration corresponds to the equilibrium state. Therefore, one would expect that the system remains in its initial state for all time. However, the equilibrium is unstable and a small perturbation will drive the system out of equilibrium. In fact, numerical inaccuracies suffice to start the oscillator. However, we accelerate the transient phase by perturbing  $I_L(t)$  by the value  $5 \cdot 10^{-6}$  A for  $t \leq 0$ . The numerical result is presented in Figure 15. The simulation took less than 4 hours computing time on an Intel Core 2 Quad Core Q9950 with  $4 \times 2.8$  GHz.

## REFERENCES

- [1] A. Arnold. Numerically absorbing boundary conditions for quantum evolution equations. *VLSI Design* 6 (1998), 313–319.
- [2] A. Arnold. Mathematical concepts of open quantum boundary conditions. *Trans. Theory Stat. Phys.* 30 (2001), 561–584.
- [3] A. Arnold, M. Ehrhardt, and I. Sofronov. Discrete transparent boundary conditions for the Schrödinger equation: Fast calculation, approximation, and stability. *Commun. Math. Sci.* 1 (2003), 501–556.
- [4] V. A. Baskakov and A. V. Popov. Implementation of transparent boundaries for numerical solution of the Schrödinger equation. *Wave Motion* 14 (1991), 123–128.
- [5] N. Ben Abdallah and A. Faraj. An improved transient algorithm for resonant tunneling. Preprint, Université Paul Sabatier, Toulouse, France. <http://arxiv.org/abs/1005.0444>, May 2010.
- [6] N. Ben Abdallah and O. Pinaud. Multiscale simulation of transport in an open quantum system: Resonances and WKB interpolation. *J. Comput. Phys.* 213 (2006), 288–310.
- [7] B. Biegel. Wigner function simulation of intrinsic oscillations, hysteresis, and bistability in resonant tunneling structures. *SPIE Proceedings: Ultrafast Phenomena in Semiconductors II* 3277 (1998), 159–169.
- [8] V. Bonnaillie-Noël, A. Faraj, and F. Nier. Simulation of resonant tunneling heterostructures: numerical comparison of a complete Schrödinger-Poisson system and a reduced nonlinear model. *J. Comput. Electr.* 8 (2009), 11–18.

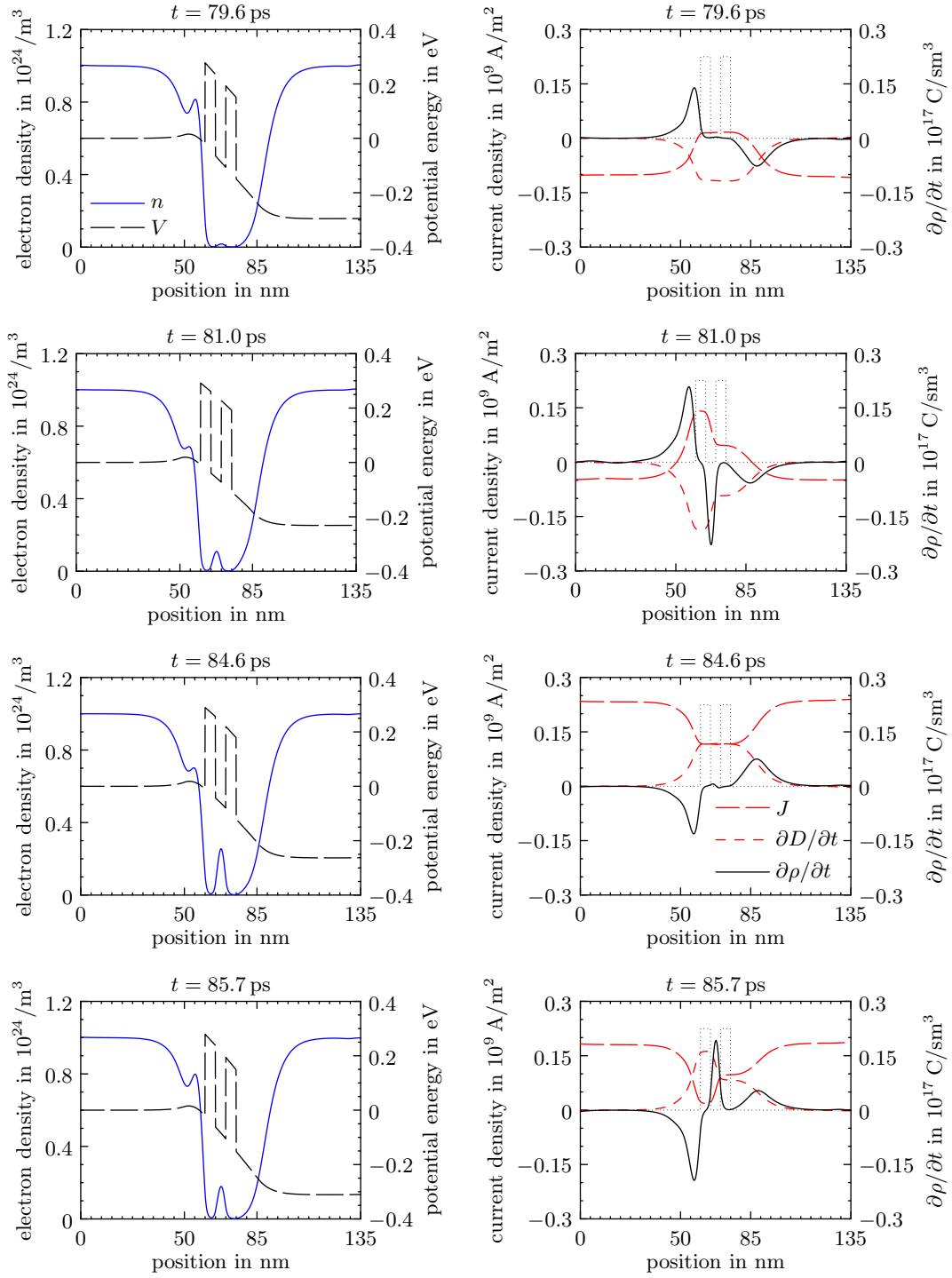


FIGURE 14. First circuit simulation: Electron density, potential energy, current densities, and variation of the electron density versus position in the RTD at four different times.

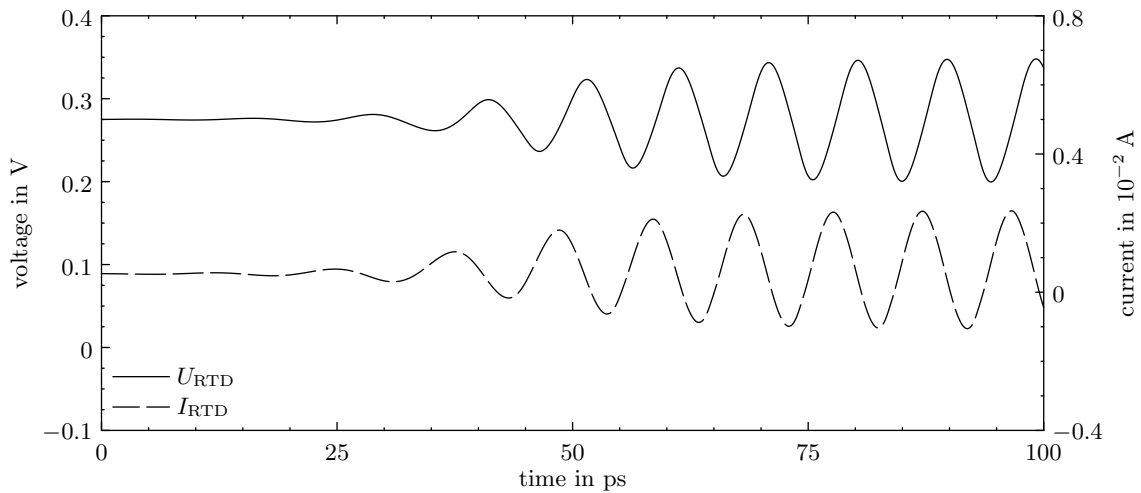


FIGURE 15. Second circuit simulation: Applied voltage and current at the resonant tunneling diode versus time.

- [9] E. Brown, J. Söderström, C. Parker, L. Mahoney, K. Molvar, and T. McGill. Oscillations up to 712 GHz in InAs/AlSb resonant-tunneling diodes. *Appl. Phys. Lett.* 58 (1991), 2291–2293.
- [10] S. Datta. A simple kinetic equation for steady-state quantum transport. *J. Phys.: Condens. Matter* 2 (1990), 8023–8052.
- [11] M. Ehrhardt and A. Arnold. Discrete transparent boundary conditions for the Schrödinger equation. *Revista Mat. Univ. Parma* 6 (2001), 57–108.
- [12] C. Gardner. The quantum hydrodynamic model for semiconductor devices. *SIAM J. Appl. Math.* 54 (1994), 409–427. (English)
- [13] X. Hu, S.-Q. Tang, and M. Leroux. Stationary and transient simulations for a one-dimensional resonant tunneling diode. *Commun. Comput. Phys.* 4 (2008), 1034–1050.
- [14] B. Jacob, G. Guennebaud et al. **Eigen**, Version 3. <http://eigen.tuxfamily.org>, 2010.
- [15] F. Johansson et al. **mpmath**: a Python library for arbitrary-precision floating-point arithmetic (version 0.15). <http://code.google.com/p/mpmath>, June 2010.
- [16] A. Jüngel, D. Matthies, and J.-P. Milišić. Derivation of new quantum hydrodynamic equations using entropy minimization. *SIAM J. Appl. Math.* 67 (2006), 46–68.
- [17] A. Khan, P.K. Mahapatra, and C.L. Roy. Lifetime of resonant tunnelling states in multibarrier systems. *Phys. Lett. A* 249 (1998), 512–516.
- [18] G. Klimeck, R. L. Lake, R. C. Bowen, W. R. Frensley, and T. Moise. Quantum device simulation with a generalized tunneling formula. *Appl. Phys. Lett.* 67 (1995), 2539–2541.
- [19] N. C. Kluksdahl, A. M. Kriman, D. K. Ferry, and C. Ringhofer. Self-consistent study of the resonant-tunneling diode. *Phys. Rev. B* 39 (1989), 7720–7735.
- [20] N. M. Kriplani, S. Bowyer, J. Huckaby, and M. B. Steer. Modelling of an Esaki tunnel diode in a circuit oscillator. *Active Passive Electr. Components* 2011 (2011), Article ID 830182, 8 pages.
- [21] W.-R. Liou, J.-C. Lin, and M.-L. Yeh. Simulation and analysis of a high-frequency resonant tunneling diode oscillator. *Solid-State Electr.* 39 (1996), 833–839.
- [22] O. Pinaud. Transient simulations of a resonant tunneling diode. *J. Appl. Phys.* 92 (2002), 1987–1994.
- [23] M. A. Talebian and W. Pötz. Open boundary conditions for a time-dependent analysis of the resonant tunneling structure. *Appl. Phys. Lett.* 69 (1996), 1148–1150.
- [24] N. Muramatsu, H. Okazaki, and T. Waho. A novel oscillation circuit using a resonant-tunneling diode. *Circuits and Systems, 2005. ISCAS 2005. IEEE International Symposium on* 3 (2005), 2341–2344

INSTITUTE FOR ANALYSIS AND SCIENTIFIC COMPUTING, VIENNA UNIVERSITY OF TECHNOLOGY,  
WIEDNER HAUPTSTRASSE 8–10, 1040 WIEN, AUSTRIA

*E-mail address:* mennemann@asc.tuwien.ac.at

INSTITUTE FOR ANALYSIS AND SCIENTIFIC COMPUTING, VIENNA UNIVERSITY OF TECHNOLOGY,  
WIEDNER HAUPTSTRASSE 8–10, 1040 WIEN, AUSTRIA

*E-mail address:* juengel@tuwien.ac.at

INSTITUTE FOR MICROELECTRONICS, VIENNA UNIVERSITY OF TECHNOLOGY, GUSSHAUSSTRASSE 27–  
29, 1040 WIEN, AUSTRIA

*E-mail address:* kosina@iue.tuwien.ac.at